

Muon Scattering Tomography for Non-Destructive Testing of High Z Materials: An Experimental and a Simulation Study with Geant4

Ramkrishna Joshi

A Dissertation Submitted to
Indian Institute of Technology Hyderabad
In Partial Fulfillment of the Requirements for the Degree of
Master of Science



భారతీయ సౌంకేతిక విజ్ఞాన సంస్థ ప్రైస్టర్ రాబాద్
भारतीय प्रौद्योगिकी संस्थान हैदराबाद
Indian Institute of Technology Hyderabad

Advisor: Dr. Saurabh Sandilya

Department of Physics
Indian Institute of Technology Hyderabad
May 30, 2025

Declaration

I declare that this written submission represents my ideas in my own words, and where ideas or words of others have been included, I have adequately cited and referenced the original sources. I also declare that I have adhered to all principles of academic honesty and integrity and have not misrepresented or fabricated or falsified any idea/data/fact/source in my submission. I understand that any violation of the above will be a cause for disciplinary action by the Institute and can also evoke penal action from the sources that have thus not been properly cited, or from whom proper permission has not been taken when needed.



Ramkrishna Joshi
(PH23MSCST11029)

Approval Sheet

This thesis entitled “**Muon Scattering Tomography for Non-Destructive Testing of High Z Materials: An Experimental and a Simulation Study with Geant4**” by **Ramkrishna Joshi** is approved for the degree of Master of Science from IIT Hyderabad.



Dr. Saranya Ghosh
Department of Physics
Examiner

Dr. Saurabh Sandilya
Department. of Physics
Advisor

Acknowledgment

I would like to sincerely thank Dr. Saurabh Sandilya for his invaluable guidance throughout the project and Dr. Saranya Ghosh for thoroughly examining my work and giving valuable suggestions for the future scope of this work. A big thank you to Hridey, Vismaya, Hrishikesh and Nihar for helping me with Geant4 related difficulties and providing me lab access whenever required. I would also like to extend my sincere gratitude to the Civil Engineering Department at IIT Hyderabad for providing us with the fiber integrated concrete slabs which have been instrumental for conducting our experiments. Finally, I am indebted to my family and friends for their unwavering support and motivation,

Abstract

Muon Scattering Tomography (MST) is an emerging technique for the three-dimensional imaging of obstructive materials. In this work, we present a systematic methodology to apply MST for the non-destructive testing of high-Z materials. We perform a detailed experimental study of muon flux reduction through concrete blocks as obstructive targets. To validate the experimental findings, Geant4-based simulations of muon scattering through concrete blocks of 10 cm, 15, 18.3 cm, and 20 cm thickness, and lead blocks of 5 cm, 7 cm, 9 cm, and 11 cm thickness are performed. In depth investigation of MST with no defect targets and targets with complete and partial circular defects is presented. Furthermore, we provide description of the experimental setup, offering a comprehensive investigation of the measurement techniques and analysis framework employed. Our results highlight the effectiveness of MST for characterizing dense materials with varying compositional properties and mapping out defects in internal volumes of these materials.

Contents

Declaration	i
Approval Sheet	ii
Acknowledgment	iii
Abstract	iv
List of Figures	vi
List of Tables	vii
1 Observing subatomic particles with cloud chambers	1
1.1 Introduction	1
1.2 Principle of Operation	1
1.2.1 The Process of Supersaturation	2
1.2.2 Ionization and Particle Tracks	2
1.3 Procedure for Building Cloud Chamber	3
1.3.1 Materials Needed	3
1.3.2 Steps to Construct the Cloud Chamber	4
1.4 Historical Significance	5
1.5 Modern Applications of Cloud Chambers	6
1.5.1 Cosmic Ray Observation	6
1.6 Advancements Beyond the Cloud Chamber	6
2 Muon Scattering Tomography techniques for high Z materials	7
2.1 Introduction	7
2.2 Methodology	9
2.3 Results	16
2.3.1 Detector efficiency measurements	16
2.3.2 Efficiency Analysis of Tiles as a Function of Temperature	19
2.3.3 Experimental Trials with Concrete target	25
2.4 Geant4 simulation setup for MST	27
2.4.1 Concrete target in Geant4	27
2.4.2 Lead target in Geant4	29
2.4.3 Lead slab with complete hole defect in Geant4	31
2.4.4 Lead slab with partial hole defect in Geant4	34
2.5 Comparison plots for defect cases	37
2.6 Discussion	38

List of Figures

1.1	An α track formed in a cloud chamber.	2
1.2	Multiple β tracks formed in a cloud chamber.	3
1.3	Glass tank used for the experiment.	4
1.4	Adapted experimental setup.	4
1.5	Supersaturated layer in cloud chamber.	5
1.6	Alcohol rain in cloud chamber	5
2.1	Cosmic ray shower schematic.	8
2.2	MST and MSA application .	8
2.3	SiPM coupled plastic scintillator.	9
2.4	CAEN cosmic hunter system.	10
2.5	Setup for detector efficiency measurements.	10
2.6	Concrete target blocks.	11
2.7	Experimental setup for MST with and without target.	12
2.8	Geant4 simulation setup.	13
2.9	Planar muon source schematic.	14
2.10	Geant4 geometry of complete defect targets.	15
2.11	Geant4 geometry of partial defect targets.	16
2.12	ABC coincidence vs temperature plot.	17
2.13	ABC coincidence vs binned temperature plot.	17
2.14	SiPM gain variation with temperature plot.	18
2.15	Average CB coincidence vs temperature bins plot.	19
2.16	Efficiency of Tile A as a function of temperature.	20
2.17	Average AC coincidence counts vs temperature bins.	21
2.18	Efficiency of Tile B as a function of temperature.	22
2.19	Average AB coincidence counts vs temperature bins.	23
2.20	Efficiency of Tile C as a function of temperature.	24
2.21	Comparison of tile efficiencies as a function of temperature.	25
2.22	ABC coincidence count with concrete target.	26
2.23	ABC coincidence count without concrete target.	26
2.24	Overlaid plot for ABC coincidence count with and without concrete slab.	27
2.25	Simulation results for 10 cm thick concrete slab.	28
2.26	Plot for variation of muon counts with concrete slab thickness	29
2.27	Simulation results for 7 cm thick lead slab.	30
2.28	Plot for variation of muon counts with lead slab thickness.	31
2.29	Scattering patterns for complete holes.	32
2.30	Muon counts vs. complete hole radius plot.	33
2.31	Scattering patterns for partial holes.	35
2.32	Muon counts vs. partial hole radius plot.	36
2.33	Combined results for no defect, complete, and partial defect cases.	37

List of Tables

2.1	Efficiency of Tile A (ϵ_A) across temperature bins	20
2.2	Efficiency of Tile B (ϵ_B) across temperature bins	21
2.3	Efficiency of Tile C (ϵ_C) across temperature bins	23
2.4	Comparison of efficiencies ϵ_A , ϵ_B , and ϵ_C across temperature bins	24
2.5	Muon counts for concrete slab without hole (100,000 muons run)	28
2.6	Muon count for lead slab without hole (100,000 muons run)	30
2.7	Detector counts for lead slabs of 7 cm and 9 cm with defect	31
2.8	Detector counts for 7 cm lead slab with 6 cm partial defect	34
2.9	Muon counts for 7 cm lead slab with 5 cm partial defect	34

Chapter 1

Observing subatomic particles with cloud chambers

1.1 Introduction

A cloud chamber, also known as a Wilson cloud chamber, is a particle detection device that allows us to visualize the invisible paths of ionizing radiation. Developed by Scottish physicist Charles Thomson Rees Wilson in 1911, the cloud chamber is considered one of the most significant advancements in experimental physics. Cloud chambers provide a direct way to observe subatomic particles and their interactions in labs. Cloud chambers have played a crucial role in allowing scientists to investigate the behavior of alpha and beta particles, electrons, and even cosmic rays. The cloud chamber's simplicity and effectiveness made it one of the most widely used tools in particle physics in the early 20th century.

In its simplest form, a cloud chamber consists of a sealed container filled with a vapor-saturated gas, typically alcohol vapor, and maintained at a specific temperature gradient. By cooling the bottom of the chamber, a supersaturated layer of vapor is created near the cold surface. When a charged particle, such as an electron or proton, travels through the chamber, it ionizes the gas molecules along its path, leaving a trail of ions. These ions act as nucleation sites around which the vapor condenses, forming tiny droplets that reveal the trajectory of the particle. This intricate process allows us to observe and analyze the nature of the particles based on the shape and density of their tracks.

The study of particle tracks within cloud chambers led to some of the most important discoveries in modern physics. In the 1930s, physicist Carl Anderson used a cloud chamber to detect the positron, the antimatter counterpart of the electron. This was the first experimental evidence of antimatter. Cloud chambers also provided the first glimpses into cosmic radiation, high-energy particles originating from outer space. By examining the interactions of these cosmic particles within the cloud chamber, scientists discovered new types of particles and began to understand the complex processes that occur beyond Earth's atmosphere.

1.2 Principle of Operation

The operation of a cloud chamber relies on the balance between temperature, vapor saturation, and ionization. By creating a supersaturated environment within the chamber,

cloud chambers allow us to visualize the tracks of charged particles as they pass through. This is achieved by taking advantage of the tendency of certain vapors to condense into visible droplets when they encounter ions in the air. In essence, the cloud chamber works by creating a visual image and representation of ionization which is an important property of particles that enables them to strip electrons from atoms in their path.

1.2.1 The Process of Supersaturation

A cloud chamber typically consists of a sealed container in which a volatile liquid, most commonly alcohol (such as isopropyl alcohol or methanol), is vaporized. The chamber's bottom is cooled to a very low temperature using dry ice or other cooling techniques, while the upper part of the chamber remains relatively warm. This temperature gradient is key to creating a supersaturated layer of alcohol vapor near the cooled surface. When air saturated with alcohol vapor is cooled, it reaches a state of supersaturation, where the vapor is ready to condense but has not yet done so because it lacks nucleation points.

Supersaturation is a critical condition for cloud chambers. In this state, the vapor remains in gas form only because there is no suitable site to initiate condensation. When ions, which are essentially charged atoms or molecules, are introduced into this environment, they serve as nucleation points for the vapor to condense around. The temperature gradient must be carefully maintained to sustain this supersaturated environment, as any disruption can prevent the formation of visible tracks. This intricate balance demands for a careful experimentation and proper setup.

1.2.2 Ionization and Particle Tracks

As mentioned, key to visualizing particles in a cloud chamber lies in the phenomenon of ionization. Ionizing particles, such as alpha particles, beta particles (electrons), or cosmic rays, interact with the vapor molecules as they pass through the chamber, creating ions along their paths. These ions act as condensation centers, causing the vapor to condense into tiny droplets around them. This process forms visible “tracks” or “trails” that reveal the path the particle took through the chamber.

Each type of particle leaves a characteristic trail based on its energy, mass, and charge:

- **Alpha Particles:** These are relatively heavy, positively charged particles consisting of two protons and two neutrons. Because of their large mass, alpha particles move relatively slowly and interact heavily with the vapor molecules, creating thick, straight, and easily visible tracks.



Figure 1.1: An α track formed in a cloud chamber. Video Courtesy: Harvard Natural Sciences Lecture Demonstrations

- **Beta Particles:** Beta particles, or electrons, are much lighter and carry a negative charge. Due to their small mass, they tend to be deflected easily by collisions with molecules in the vapor, resulting in thin, zigzag tracks that show their paths through the chamber.



Figure 1.2: Multiple β tracks formed in a cloud chamber. Video Courtesy: Harvard Natural Sciences Lecture Demonstrations

- **Cosmic Rays and Other High-Energy Particles:** High-energy particles from cosmic rays or other sources can also be detected in a cloud chamber. These particles may create very long, thin, and straight tracks, as they move at high speeds and tend to ionize fewer molecules along their paths.

1.3 Procedure for Building Cloud Chamber

Building a basic cloud chamber is possible with a few materials. The following procedure describes how to create a simple cloud chamber in a lab or a classroom setting.

1.3.1 Materials Needed

- Clear plastic/glass container (a small fish tank or glass jar works well)
- Metal tray (preferably black painted)
- Heating Pad/Bag
- Black felt (for the base)
- Isopropyl alcohol (IPA: 99% preferred)
- Dry ice (solid carbon dioxide)
- Heat-resistant gloves
- Neodymium magnets
- Flashlight

1.3.2 Steps to Construct the Cloud Chamber

1. **Prepare the Base:** Attach a black felt to the top of the glass/plastic container by using magnets . For this experiment we have considered a 22/14/15 inch glass tank.



Figure 1.3: Glass tank used for the experiment

2. **Add the Alcohol:** Soak the felt material with IPA. The alcohol vapor will gradually saturate the air inside the chamber.



Figure 1.4: Adapted experimental setup

3. **Cooling the Chamber:** Carefully place the container on black painted metal tray and place the assembly on dry ice, using gloves for safety. The cold temperature will cause the alcohol vapor to cool rapidly, creating a supersaturated layer near

the bottom of the chamber.



Figure 1.5: Supersaturated layer formed near the bottom of the cloud chamber

4. **Seal the Chamber:** Seal the container completely at the container-tray contact to ensure that the vapor layer does not escape the container. Allow a few minutes for the chamber to stabilize and for the supersaturated vapor layer to form near the bottom.
5. **Observing the Tracks:** Shine a flashlight at an angle into the chamber to make any particle tracks more visible. As cosmic rays or other ionizing particles pass through the chamber, they will create visible condensation trails that can be observed and studied.



Figure 1.6: With appropriate experimental measures and care, particle tracks can possibly originate in the alcohol rain. Alcohol rain can be observed in the image but particle tracks are not seen in these images.

1.4 Historical Significance

The cloud chamber was crucial in early particle physics research concerning discoveries of new charged particles and study of their properties and interactions.

The cloud chamber also played a role in understanding cosmic radiation. Through observations of particle interactions within cloud chambers, physicists discovered new types of particles and their behavior.

1.5 Modern Applications of Cloud Chambers

Although more advanced particle detectors, such as bubble chambers and wire chambers, are widely used now a days in high-energy physics research, cloud chambers are still used today in educational demonstrations and certain types of laboratory research.

1.5.1 Cosmic Ray Observation

Cloud chambers can detect cosmic rays at ground level, making them valuable tools in astro-particle physics. By observing cosmic ray interactions, scientists can gain insights into high-energy particles from space and the types of interactions they undergo upon entering Earth's atmosphere.

1.6 Advancements Beyond the Cloud Chamber

While cloud chambers were revolutionary in their time, new technologies have since taken over in particle detection. Bubble chambers, developed in the 1950s, allowed scientists to observe particle interactions at even higher energies. These chambers use superheated liquid rather than vapor and can record particle paths more efficiently than cloud chambers.

Wire chambers, another counterpart to cloud chambers, use a grid of wires to detect ionized particles in real time and have played a crucial role in large-scale particle physics experiments, such as those conducted at CERN.

Chapter 2

Muon Scattering Tomography techniques for high Z materials

2.1 Introduction

Muon Scattering Tomography (MST) is an advanced imaging technique that leverages the natural flux of cosmic muons to non-destructively probe the internal structure of dense objects. Unlike traditional radiographic methods, MST exploits the multiple Coulomb scattering of muons as they traverse materials, making it particularly sensitive to variations in atomic number (Z) and density. This unique sensitivity enables MST to distinguish between materials of different compositions, offering a significant advantage for the characterization of high- Z substances such as lead, uranium, and tungsten.

High- Z materials, due to their large atomic numbers, cause greater deflections in the trajectories of incoming muons. By measuring the scattering angles of muons after they interact with the target, MST can reconstruct three-dimensional maps of the internal structure of the material. These reconstructions provide information about the density variations inside the target volume, making MST an invaluable tool for a wide range of applications.

Cosmic muons are secondary particles produced when high-energy cosmic rays—primarily protons and heavier nuclei—collide with atomic nuclei in the Earth’s upper atmosphere. These collisions initiate extensive air showers, generating a cascade of particles, including charged pions (π^\pm) and kaons (K^\pm). These unstable mesons subsequently decay into muons and neutrinos via weak interactions, such as $\pi^\pm \rightarrow \mu^\pm + \nu_\mu(\bar{\nu}_\mu)$. Muons (μ^\pm) are leptons with a mass of approximately $105.7 \text{ MeV}/c^2$, about 200 times heavier than electrons. Despite being unstable, muons have a relatively long lifetime of about 2.2 microseconds in their rest frame, allowing them to travel significant distances—several kilometers in the atmosphere—before decaying into electrons and neutrinos. Their high penetration capability makes muons ideal probes for muon scattering tomography, a technique that utilizes naturally occurring cosmic muons to investigate the internal structure of large and dense objects. By tracking the deflection angles of muons as they pass through different materials, this method enables non-invasive imaging of otherwise inaccessible structures such as nuclear reactors, geological formations, and even ancient pyramids.

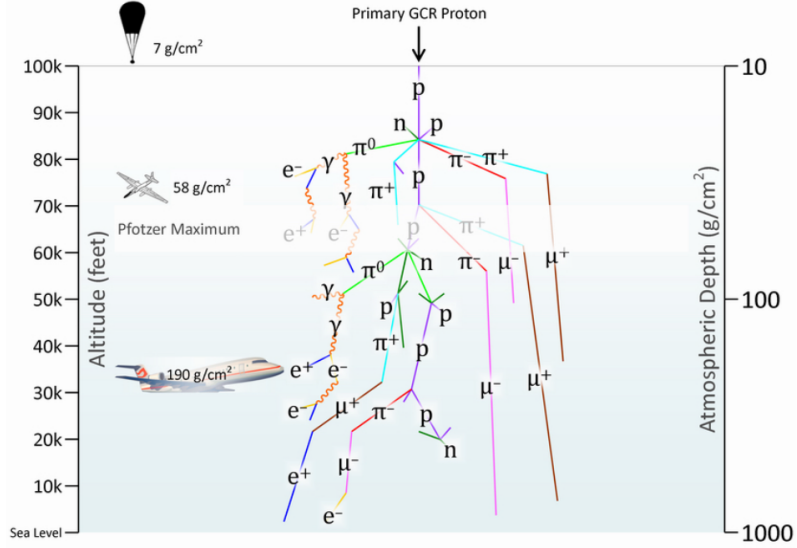


Figure 2.1: Cosmic ray shower with atmospheric depth markers showing atmospheric depths at which fundamental particles originate. Source: Oklahoma State University, Department of Physics – Dr. Benton’s Lab: Studies in Cosmic Ray Muons.

The use of MST has shown great potential in fields such as national security (e.g., detection of concealed nuclear materials), geological surveying (e.g., imaging volcanic interiors), and civil engineering (e.g., structural health monitoring). In particular, MST offers a promising non-invasive method for defect detection within high- Z materials and dense structures, where conventional techniques may fall short due to limited penetration depth or safety concerns.

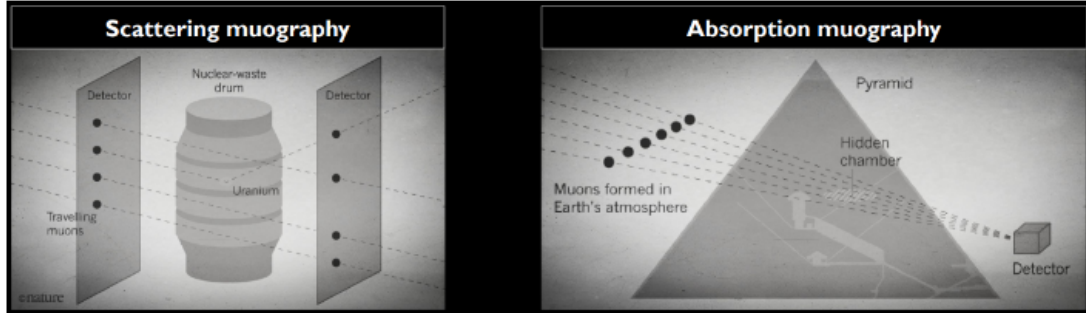


Figure 2.2: Application of Muon Scattering Tomography (MST) lies in mapping nuclear waste containers and contraband detection. Muon Absorption Tomography (MAT) has been applied for mapping out the internal volumes of pyramids and volcanoes. Source: Lagrange, M. (2024). Introduction to Muography. École Européenne Bruxelles III

As muons traverse a material, they experience Multiple Coulomb Scattering (MCS), which arises from repeated deflections due to interactions with atomic nuclei. This scattering leads to a distribution of angular deviations from the muons' initial trajectories. The root-mean-square (RMS) scattering angle θ_0 is approximately given by [10]:

$$\theta_0 = \frac{13.6 \text{ MeV}}{\beta p z} \sqrt{\frac{x}{X_0}} \left(1 + 0.038 \ln \left(\frac{x}{X_0} \right) \right)$$

where p is the muon momentum, x is the thickness of the material, X_0 is the radiation length of the material, and β is the velocity of the muon relative to the speed of light. Materials with higher atomic number (Z) exhibit shorter radiation lengths and therefore produce greater scattering, making MCS a powerful tool for distinguishing between different materials.

Muon Scattering Tomography (MST) techniques leverage this principle by tracking multiple muon paths and analyzing their angular deviations to reconstruct 3D images of the internal structure of objects, including detecting hidden high-Z materials or defects.

This work explores the implementation of MST for the non-destructive testing of high-Z reinforced concrete and lead. We present both experimental measurements and simulation results to validate the effectiveness of MST in mapping three-dimensional volumes and identifying potential defects within materials of varying thickness and composition.

2.2 Methodology

This work has two main components namely the experimental study with fiber reinforced concrete and a simulation study with concrete and lead class in Geant4.

The experimental setup uses CAEN SP5620CH Cosmic Hunter ,a setup for cosmic-ray detection using plastic scintillator tiles coupled to Silicon Photomultipliers (SiPMs) [7]. The main components of the system include:

- **Detection Systems (SP5622):** Three detection units consisting of $15\text{ cm} \times 15\text{ cm} \times 1\text{ cm}$ polystyrene-based plastic scintillators directly coupled to AdvanSiD NUV4S-P SiPMs ($4\text{ mm} \times 4\text{ mm}$ active area). These scintillators exhibit high light output (60% of anthracene) with a fast decay time (3.3 ns), optimized for cosmic ray detection.
- **Coincidence Module (SP5621):** An ESP32-based microcontroller module that powers the scintillators, processes signals, and records single and coincidence events between tiles. It allows real-time monitoring via an integrated display and supports microSD card data storage in CSV format.

The system supports flexible configurations for various cosmic ray experiments, including single-tile and double-tile (coincidence) setups. Coincidence measurements greatly reduce random noise by only recording events that simultaneously trigger two or three scintillators, thus enhancing the muon detection accuracy. The coincidence module plays a crucial role in our experimental setup.

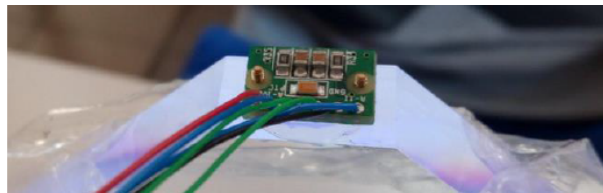


Figure 2.3: An example of a coupling used between SiPM and Plastics Scintillator. Source: Guide GD7686 SP5620CH Cosmic Hunter Rev. 1 (2021)

The Cosmic Hunter setup enables a wide range of experiments such as muon flux measurement, zenith angle dependence studies, random coincidence evaluation, absorption measurements through dense materials, and environmental radiation monitoring, making it highly suitable for applications in muon scattering tomography (MST).



Figure 2.4: Figure shows the cosmic hunter detector system to detect and study the cosmic rays. On the left is the coincidence module, and on the right are the detection systems. Source: Guide GD7686 SP5620CH Cosmic Hunter Rev. 1 (2021)

We start with characterizing the detector and measuring net gross and individual detection efficiency of each subunit of the detection system. We study the effect of temperature, humidity and pressure on the detection efficiency of the device.

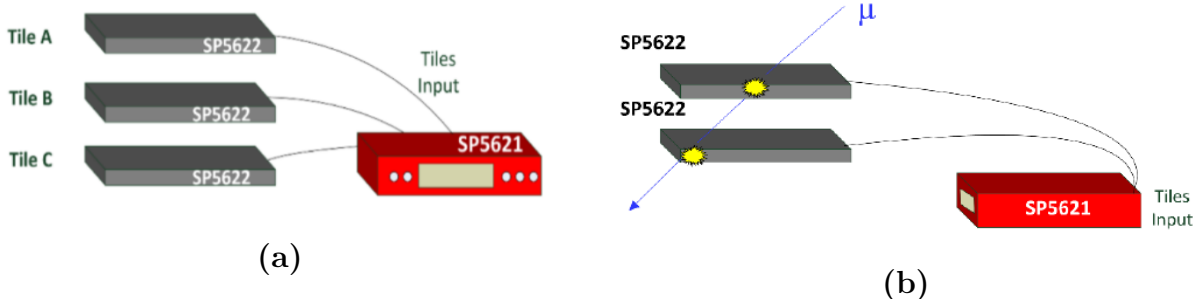


Figure 2.5: Figure shows schematic of the setup for measuring efficiency of each detector tile and the gross efficiency of the system. Panel (a) shows the triple coincidence arrangement and panel (b) shows double coincidence arrangement. Source: Guide GD7686 SP5620CH Cosmic Hunter Rev. 1 (2021)

The methodology for detector efficiency measurement proceeds as follows:

- Three detectors, labeled A, B, and C, are stacked vertically. The number of detected muons in the P^{th} detection cycle under a triple coincidence condition is given by:

$$N_P^{(3)} = N_0 \epsilon_i \epsilon_j \epsilon_k$$

where:

- N_0 is the initial number of muons reaching the topmost detector (approximately 1 muon/cm²/min),
- $N_P^{(3)}$ is the number of muons detected after triple coincidence,
- $\epsilon_{i/j/k}$ are the detection efficiencies of the i^{th} , j^{th} , and k^{th} detectors, respectively.

- To eliminate dependence on the unknown N_0 , double coincidences between pairs of detectors (ij, ik, jk) are also measured. For double coincidence between detectors i and j , the detected muons in the P^{th} cycle are given by:

$$N_P^{(2)} = N_0 \epsilon_i \epsilon_j$$

- The detection efficiency of the k^{th} detector can thus be determined by the ratio:

$$\frac{N_P^{(3)}}{N_P^{(2)}} = \epsilon_k$$

where the double coincidence measurement involves detectors i and j , and the triple coincidence measurement involves all three detectors.

- Specifically, the detection efficiency of detector A can be obtained by taking the ratio of the ABC triple coincidence to the BC double coincidence. Similarly, efficiencies for detectors B and C can be derived using appropriate pair and triple coincidence combinations.

This method for detection efficiency calculations is of central importance as it naturally gets rid of the dependence of detection on the initial value N_0 which is approximated to 1 muon/cm²/min. This value however, is not a constant and can vary significantly from place to place and also at different orientation of the detection setup. Hence implementing a framework which is independent of this value plays a crucial role in this work.

This is followed by MST measurements for fiber integrated concrete blocks supplied by the Civil Engineering Department at IIT Hyderabad.

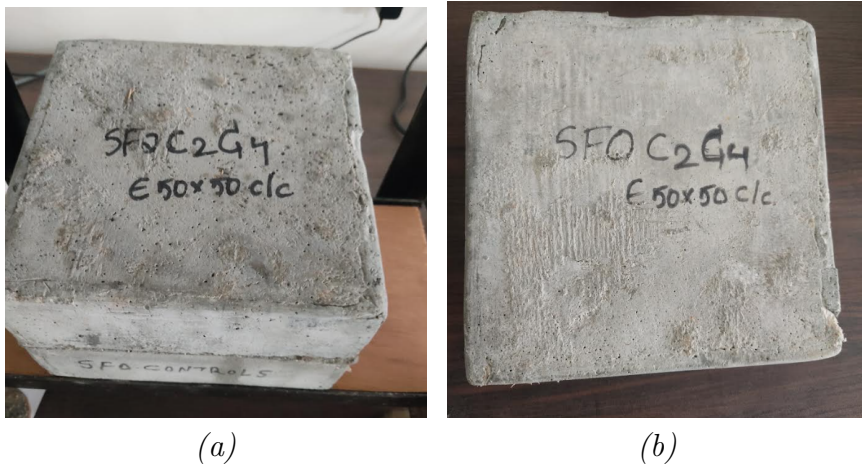


Figure 2.6: Fiber integrated concrete slabs/blocks provided by the Civil Engineering Department at IIT Hyderabad

We measure the muon flux over predetermined time frame without the concrete blocks acting as obstructions and with the concrete blocks acting as obstructions. One expects that due to scattering of muons from the concrete blocks the coincidence count in the latter case should be lower than the former.



Figure 2.7: Figure shows experimental setup for studying MST through high Z fiber integrated concrete slabs. Left panel shows muon flux measurements without the concrete slab acting as an obstruction and the right panel shows muon flux measurements with concrete slabs acting as obstructions.

For this setup, we keep the mode of detection on triple coincidence. Only those muons are counted which pass through the top as well as the bottom two detectors. This is implemented to make sure that we get confirmed MST measurement with the concrete blocks acting as obstruction. Any other mode of coincidence will include false positive count for MST muons thus giving wrong results.

The last step involves Geant4 simulation with concrete and lead blocks to verify the experimental results and pave way for future highly accurate experimental methodologies. The Geant4 simulation is based upon perpendicular incidence of muons on the setup with two detectors prior to the target and two detectors past to the target. These detectors, are scintillation detectors defined by `G4_PLASTIC_SC_VINYLTOLUENE` class. In Geant4, `G4_PLASTIC_SC_VINYLTOLUENE` refers to a predefined material based on polyvinyltoluene, a widely used plastic scintillator. This material is designed to simulate the behavior of organic scintillators that emit visible light when traversed by ionizing radiation. In detector simulations, it serves as the active medium that converts the kinetic energy of charged particles into scintillation photons, which can then be detected by optical sensors such as photomultiplier tubes or silicon photomultipliers (SiPMs). The use of `G4_PLASTIC_SC_VINYLTOLUENE` allows Geant4 to model this light generation and propagation realistically, enabling accurate studies of timing, energy deposition, and event reconstruction in particle physics experiments.

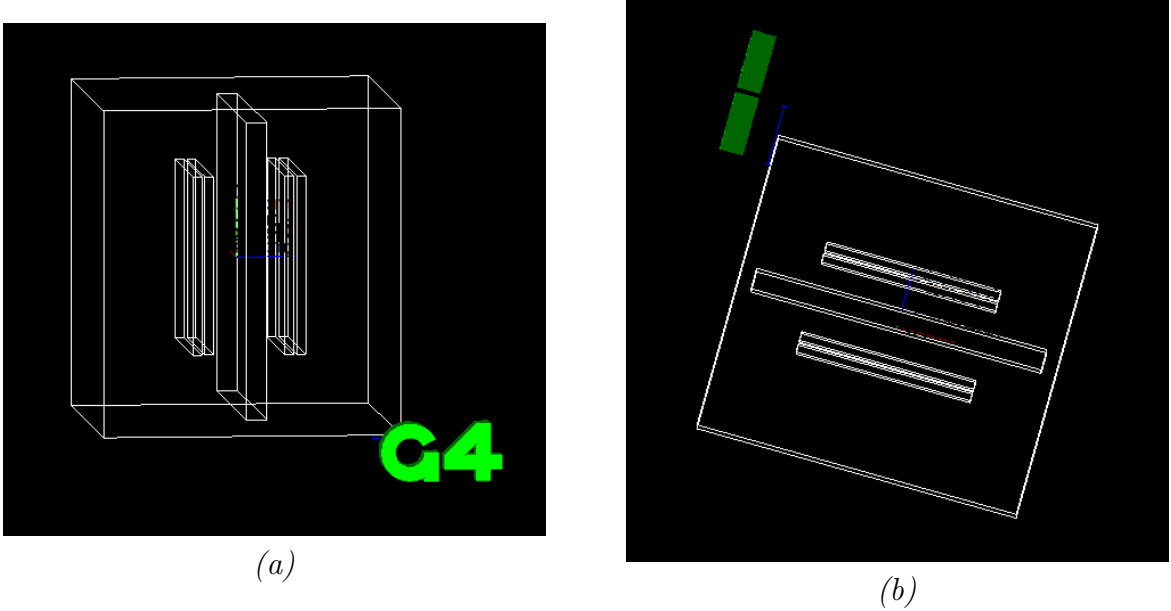


Figure 2.8: Views of the detector setup used in the simulation. Panel (a) shows the side view and panel (b) shows the top view.

The Geant4 detector geometry was implemented in the `DetectorConstruction` class. The simulation world is defined as a cubic volume filled with `G4_Galactic` material to represent vacuum, with dimensions $1.1 \text{ m} \times 1.1 \text{ m} \times 1.0 \text{ m}$. Within this world volume, a central target made of `G4_CONCRETE` (cement block) is placed at $z = 2 \text{ cm}$ and has dimensions $1.0 \text{ m} \times 1.0 \text{ m}$ with varying thickness. Another target of `G4_Pb` (lead block) with dimensions of $1.0 \text{ m} \times 1.0 \text{ m}$ also with varying thickness is used.

Surrounding the target, four identical detector volumes are defined using the plastic scintillator material `G4_PLASTIC_SC_VINYLTOLUENE`. These detectors are used to register ionizing particles that pass through or scatter from the target. Two top detectors are placed at $z = 20 \text{ cm}$ and $z = 24 \text{ cm}$, while two bottom detectors are placed symmetrically below the target at $z = -18 \text{ cm}$ and $z = -22 \text{ cm}$. Each detector has a square cross-section of $0.6 \text{ m} \times 0.6 \text{ m}$ and a thickness of 3 cm . All volumes are implemented using `G4Box` shapes and positioned with `G4PVPlacement` without any rotations.

The macro file `cosmics.mac` configures the primary generator to simulate a realistic spectrum of cosmic muons. A planar source of positive muons (μ^+) is defined above the top detector, covering a $60 \times 60 \text{ cm}^2$ area and emitting muons vertically downward along the $-Z$ direction. This setup uses a power-law energy distribution with a spectral index $\alpha = -2.7$, representative of the natural cosmic ray muon spectrum:

$$\frac{dN}{dE} \propto E^\alpha = E^{-2.7}$$

where E is the muon energy. The energy range is set between 200 MeV and 10 GeV to reflect the typical energies of atmospheric muons observed at sea level. This provides a more realistic simulation of cosmic muons as they traverse the detector system.

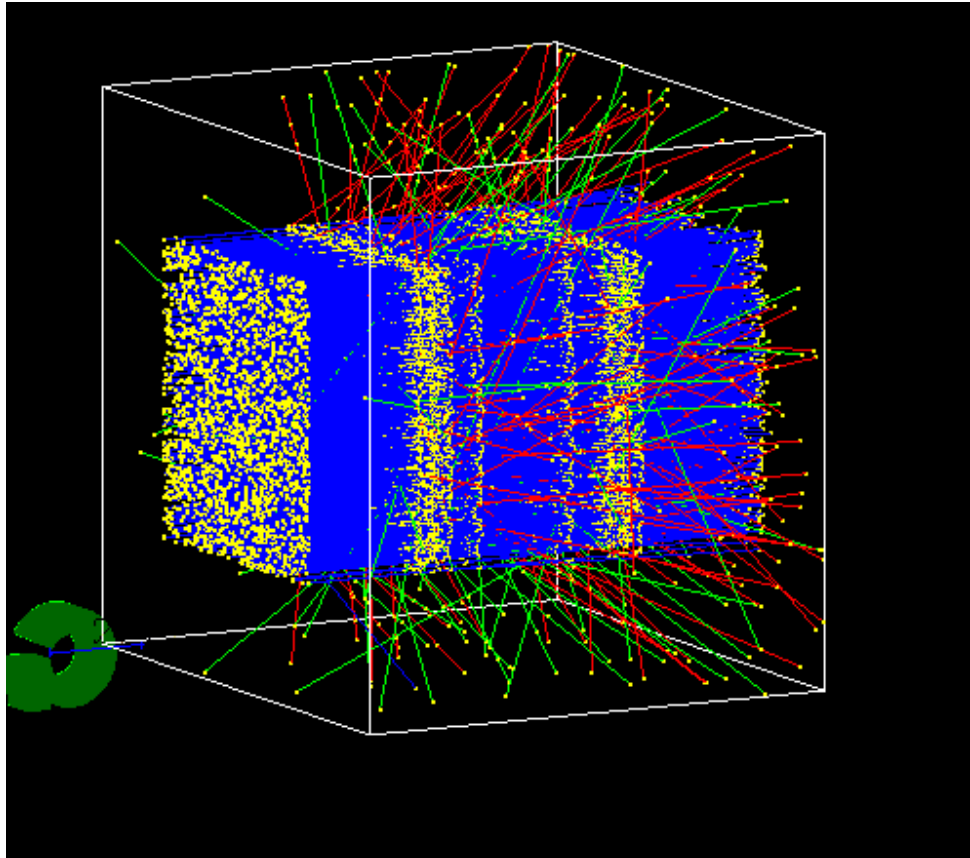


Figure 2.9: Planar muons source with a perpendicular incidence on the Top detectors. Muons scatter as they pass through the target and deposit energies. Source with 2000 Muons emitted is shown in the figure

This setup is used in Geant4 to simulate Muon Scattering Tomography techniques with different target materials. For this setup, a successful coincidence is defined when the muon passes through all four detectors. Muons deposit portion of their energy into all four detectors and target. These energy depositions can provide critical insights into the interaction of muons in the target and the detectors.

The latter step in the simulation study is understanding the muon flux distribution across the target material which has a defect in it. For a simplified, case I consider the defect to be a circular hole with varying radius. I have presented two case studies namely: a complete hole defect and partial hole defect.

- Complete Hole Defects: A complete hole defect means that the lead slab is a holed slab with the hole visible on both sides of the slab. We consider hole radii of 10 cm, 15 cm, 20 cm, 25 cm, 30 cm, 35 cm, 40 cm and 50 cm. We perform the simulation study for lead slab thickness of 7 cm and 9 cm. This study is aimed at understanding how muon flux changes with changing the dimensions of the defect. This has potential application in mapping the scattering pattern on the screen to the defect and understanding the target geometry better.

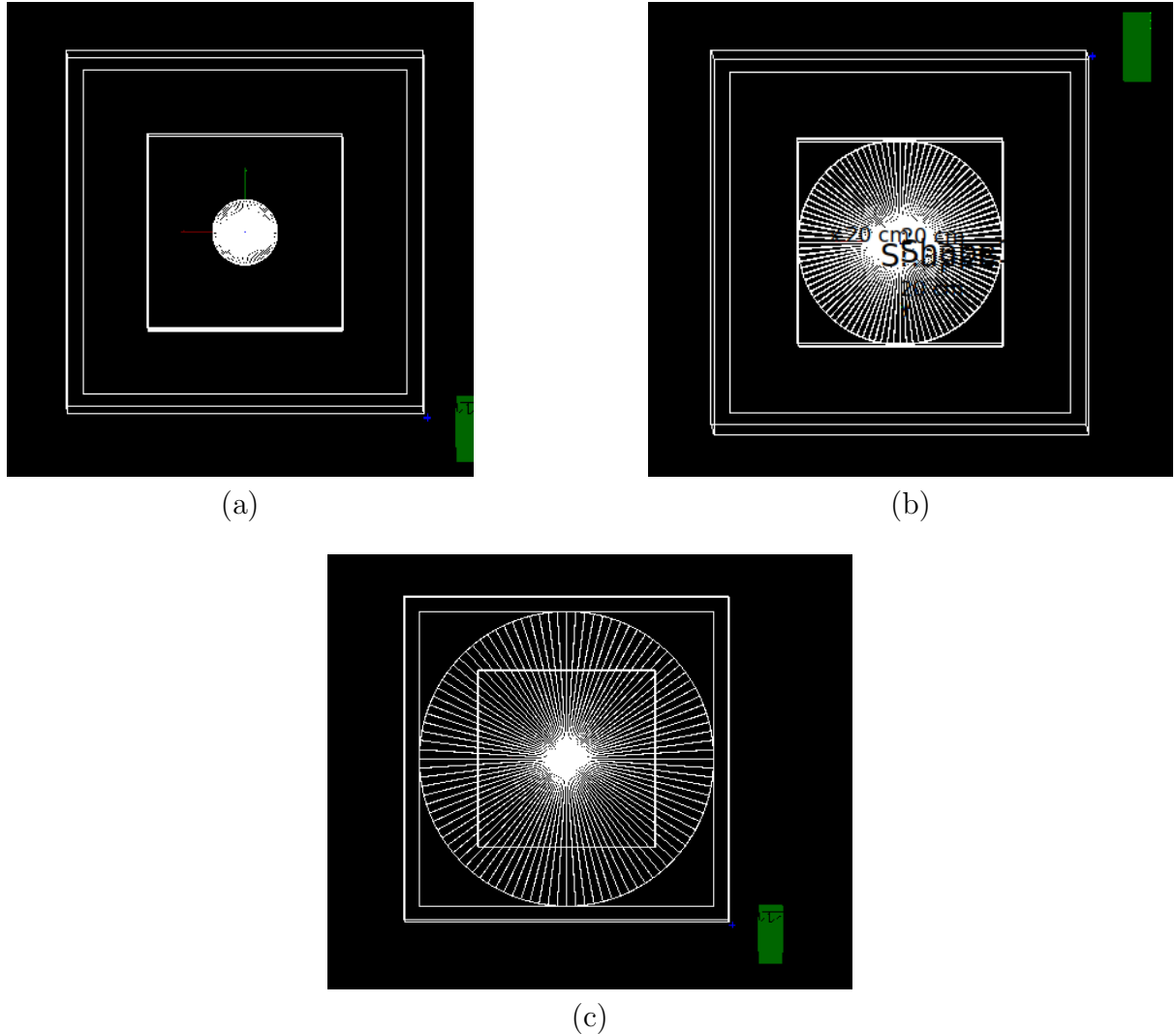


Figure 2.10: Comparison of lead slab of 7 cm thickness with central complete holes of radius (a) 10 cm, (b) 30 cm, and (c) 50 cm. Front view of the setup is shows here. The central squares represent the four detectors as seen in the front view. The second square is the lead slab as seen in the front view and the biggest square is the world in Geant4 as seen in the front view.

- **Partial Hole Defects:** A partial hole defect means that the hole is not seen on the slab but is inside the slab. We consider two cases with the hole 1 cm inside the slab i.e 0.5 cm from each end of the slab and the hole is 2 cm inside the slab i.e 1 cm from each end of the slab. With this setup also we consider hole radii of 10 cm, 15 cm, 20 cm, 25 cm, 30 cm, 35 cm, 40 cm and 50 cm. We perform the simulation study for lead slab thickness of 7 cm. This study is aimed at understanding how muon flux changes with the varying orientation and depth of the defect.

Since most of the observed targets may not have defects that are visible on the outside, this study helps better understand MST through such targets. The comparison with a complete hole defect provides important information about how variation in defect geometry, orientation and depth can influence the scattering.

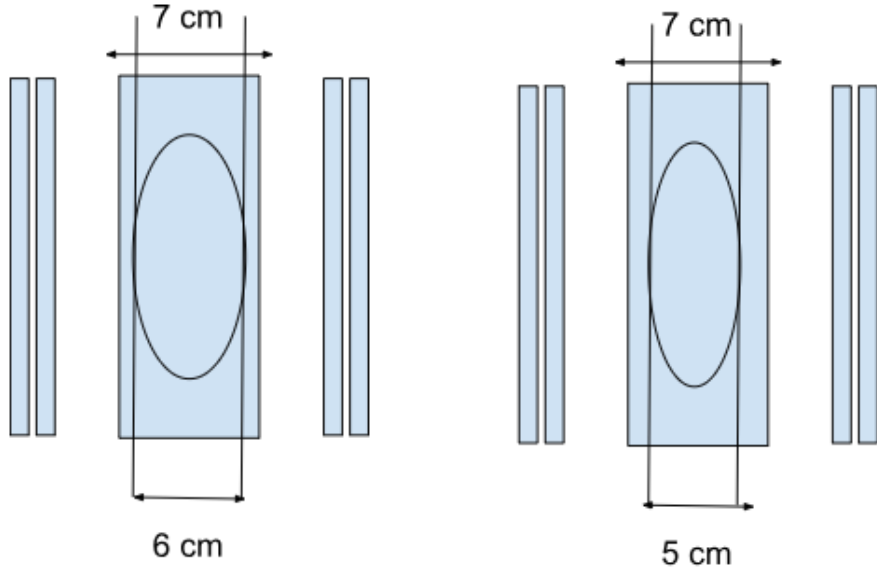


Figure 2.11: Figure shows partial hole defect geometries for partial hole 1 cm inside the lead slab (left panel) and partial hole 2 cm inside the lead slab (right panel). The oval shape represents the partial hole defect and solid lines mark the thickness of the defect. Two thin slabs on right and left sides represent the detectors and the central slab is the lead slab of 7 cm thickness.

2.3 Results

2.3.1 Detector efficiency measurements

We study the effect of humidity, temperature and pressure on the detection efficiency. Detector efficiency is seen to be affected by variations in temperature. Humidity and Pressure do not affect the sensitivity and efficiency as much as temperature does. Hence we present the efficiencies with respect to binned temperatures with each bin spanning a pre-defined temperature range. While conducting the experiment, it is necessary to conduct it within a smaller time window as to avoid major detection efficiency fluctuations as result of changing temperature. Though this is not a temperature characterization study, its important to understand the effects of temperature on detector efficiency. Since we are considering triple and double coincidence settings, one must be careful of recording the readings in the same temperature bin. One cannot compare the readings from different temperature bins for sensible conclusions. Hence, understanding the temperature effect greatly enhances the reliability of readings and their comparison.

In a typical setup, the detection efficiency of a plastic scintillator-SiPM system for vertical cosmic muons can exceed **90%**, depending on factors such as scintillator thickness, SiPM area, optical coupling, and threshold settings [25]. The overall performance of the detector can be further optimized by reducing light losses and enhancing optical matching between the scintillator and the SiPM.

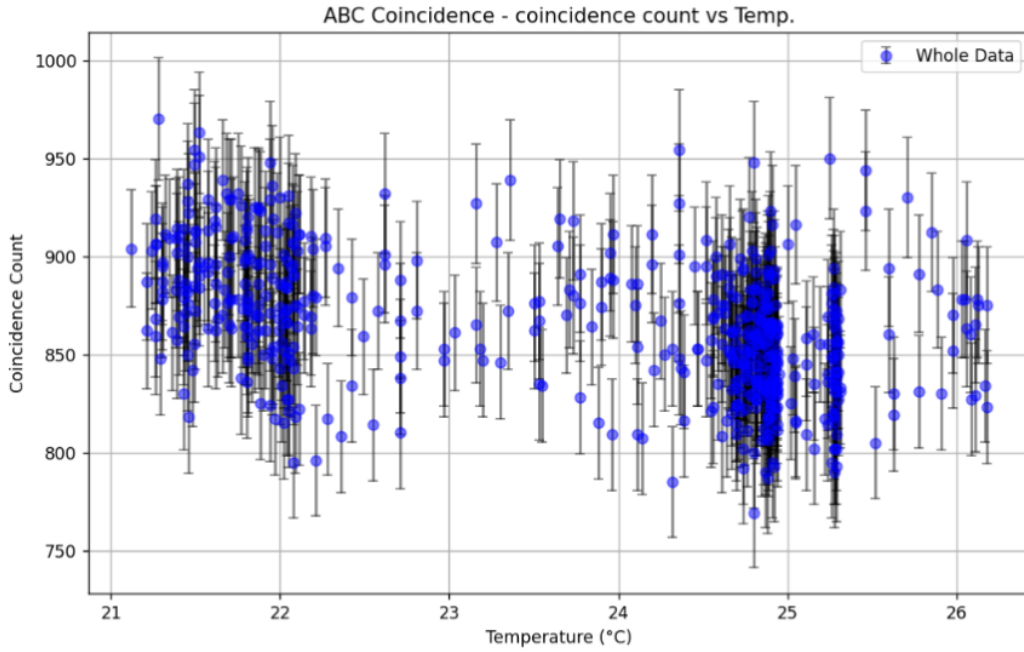


Figure 2.12: Figure shows ABC coincidence variation with temperature. Two prominent clusters of data points is observed in the plot in temperature ranges 21°C - 22°C and 24°C - 25°C .

The spearman correlation coefficient was found to be -0.448 . The two prominent cluster of data points observed is attributed to temperature variation cycles in the lab where the experiment is conducted. Due to these temperature variations, we calculate the average coincidence count for each predefined temperature bins.

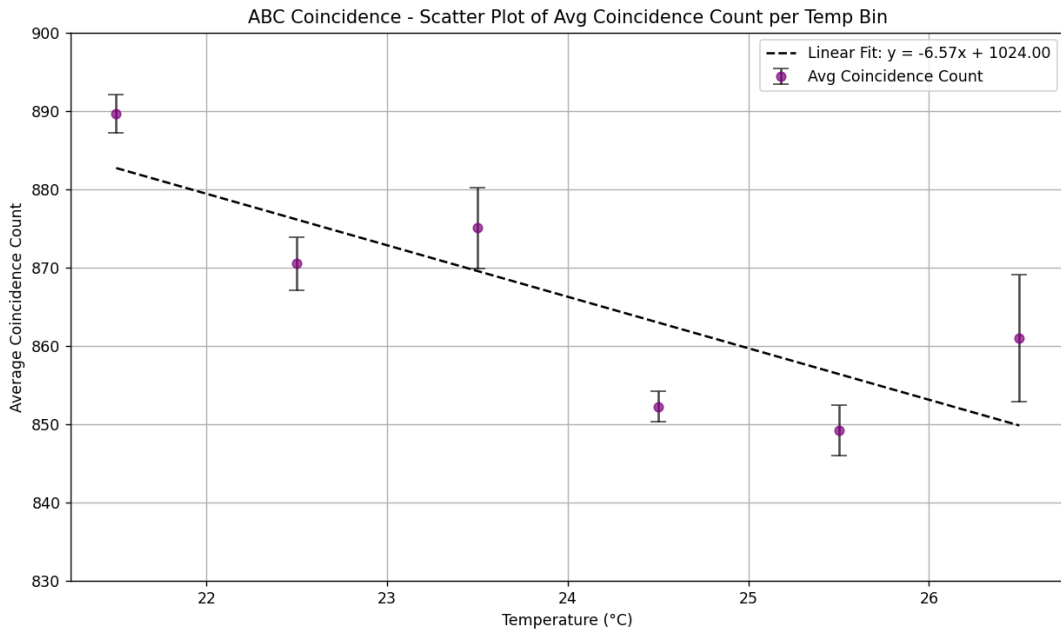


Figure 2.13: Figure shows average ABC coincidence count plotted as a function of temperature with temperature bins of 1°C . Temperatures from 21°C to 27°C are considered.

Temperature bins typically span across the temperature range of 21°C - 27°C . This temperature range is again chosen with respect to the temperature variations in the lab as a result of air conditioning. Conducting the experiment outside the lab poses major challenges of interference in the detection due to dust, physical disturbances and other environmental factors.

Overall trend points to the reducing detection efficiency with increasing temperatures. The CAEN Cosmic Hunter setup uses Silicon Photomultipliers (SiPMs) coupled to plastic scintillators to detect cosmic ray muons. The muon detection efficiency of this system decreases with increasing temperature, primarily due to the temperature-sensitive behavior of SiPMs and associated electronics. One of the main factors is the reduction in SiPM gain with temperature. The gain depends on the overvoltage, which is the difference between the applied bias voltage and the breakdown voltage. Since the breakdown voltage increases with temperature—typically by $20\text{--}50\text{ mV}/^{\circ}\text{C}$ —a fixed bias voltage results in reduced overvoltage, and therefore reduced gain. This leads to weaker output signals for the same number of incident photons, causing some muon signals to go undetected.

In addition to gain reduction, the dark count rate of SiPMs increases exponentially with temperature due to enhanced thermally-generated carriers. This raises the background noise, making it harder to distinguish real muon signals from random electronic noise. The front-end electronics used in the detection system, such as amplifiers and discriminators, may not automatically adjust to temperature-induced changes in SiPM output. Consequently, the reduced signal amplitudes at higher temperatures may not be sufficient to exceed fixed detection thresholds, further contributing to efficiency loss.

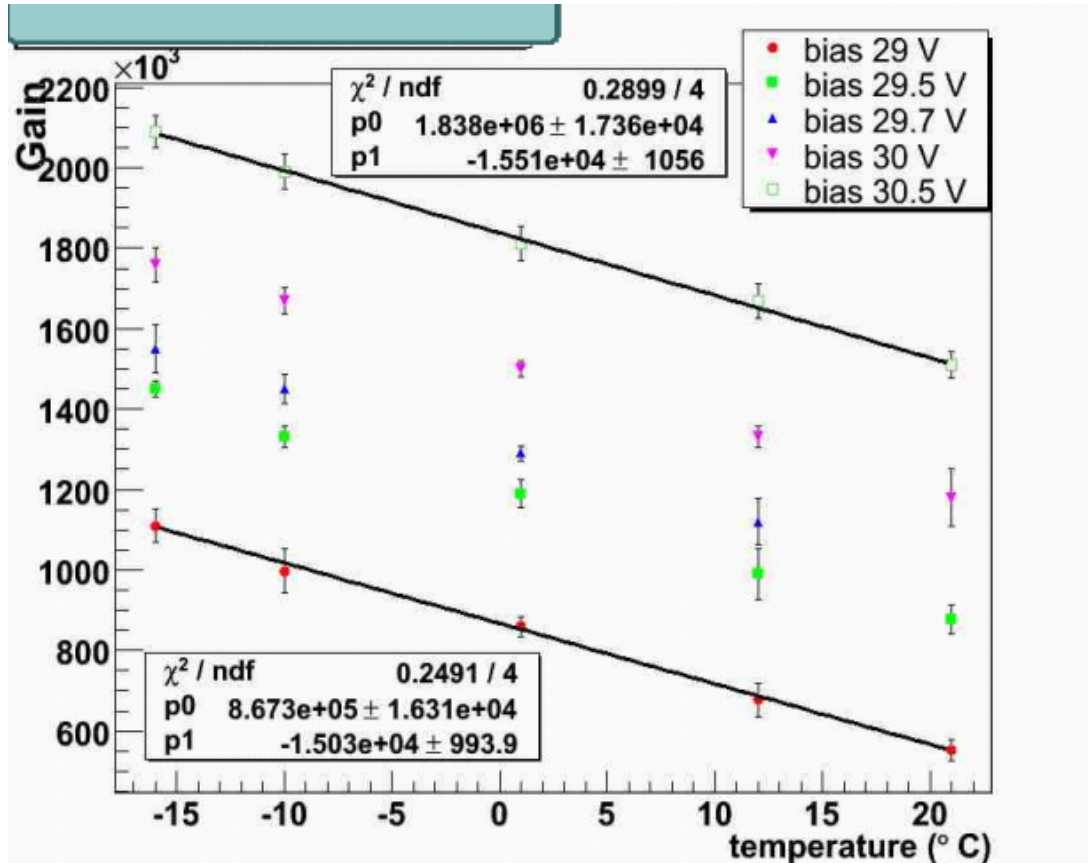


Figure 2.14: Variation of sippm gain with temperature at different bias voltages. The plot is for the sippm system without temperature compensation. Source:CAEN SiPM module

In summary, the observed decline in muon detection efficiency with rising temperature is mainly due to reduced SiPM gain, increased thermal noise, and lack of temperature compensation in the readout electronics, all of which reduce the signal-to-noise ratio and the likelihood of accurately detecting muon events. In this context, the observation of reducing detection efficiency with increasing temperatures is justified. The average ABC coincidence count does not reduce greatly over the mentioned temperature range. This is a good sign, since this simplifies the characterization of detectors at different temperatures. A greater reduction in efficiency with temperature would further restrict the temperature binning and characterization procedure rendering it very difficult to conduct the experiment over a wider temperature range.

2.3.2 Efficiency Analysis of Tiles as a Function of Temperature

The setup consists of a detection module with three detection tiles (Refer to the Methodology section for detailed review of the experimental setup). For characterizing, each of the detection tiles, detection efficiency of each tile plays a central role. In this section, we present results for detection efficiency of A,B and C tiles, following the procedure mentioned in the Methodology section.

Efficiency of Tile A

While calculating the efficiency of tile A, we need to consider two categories of readings. The first category consists of the ABC coincidence readings which consider the detection counts only when the muon has passed through all the three detector tiles A,B and C. For the double coincidence readings, we consider the CB coincidence. On taking the ratio of the triple and double coincidence readings, we obtain the efficiency of tile A.

The efficiency of Tile A is given by:

$$\epsilon_A = \frac{N(ABC, T)}{N(CB, T)}$$

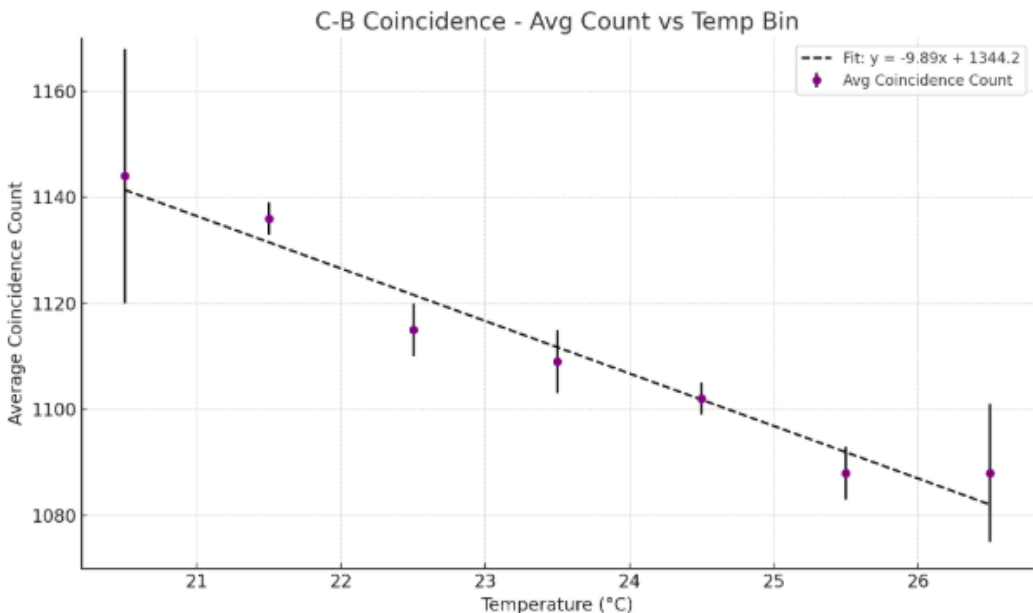


Figure 2.15: Average CB coincidence counts across temperature bins.

Overall trend shows that the CB coincidence count reduces with temperature. ABC coincidence count also reduces with temperature (Refer Fig. 2.12). Hence, practically its a little challenging to predict whether the ratio of ABC and CB will reduce or not. One can expect slight variations in the efficiency at different temperature bins.

Temperature ($^{\circ}\text{C}$)	ABC Count	CB Count	ϵ_A	$\delta\epsilon_A$
21–22	889.65 ± 2.47	1135.70 ± 2.54	0.783	0.002
22–23	870.49 ± 3.36	1114.45 ± 4.46	0.781	0.004
23–24	875.07 ± 5.15	1108.82 ± 5.80	0.789	0.007
24–25	852.27 ± 1.90	1101.62 ± 2.12	0.774	0.002
25–26	849.17 ± 3.22	1088.11 ± 4.81	0.781	0.004

Table 2.1: Efficiency of Tile A (ϵ_A) and its uncertainty across temperature bins.

As expected, slight variations and reduction is observed in the efficiency at different temperature bins. The overall trend shows that, on an average, there is a slight reduction in the detection efficiency at high temperatures. The case of the temperature bin $26^{\circ}\text{C} - 27^{\circ}\text{C}$ is a curious case, since there are relatively less number of readings in that temperature bin. This happens since less number of detection cycles fall in that temperature bin as it is achieved for a short period of time in the day. Due to air conditioning in the lab during the peak temperature periods, even though the temperatures outside might soar to 27°C and above, the temperature inside the lab remains to be slightly lower. Due to this, less number of detection cycles are recorded at higher temperatures. This might be one of the leading factors for higher efficiency readings in that temperature bin. This trend is observed generally across all detection tiles.

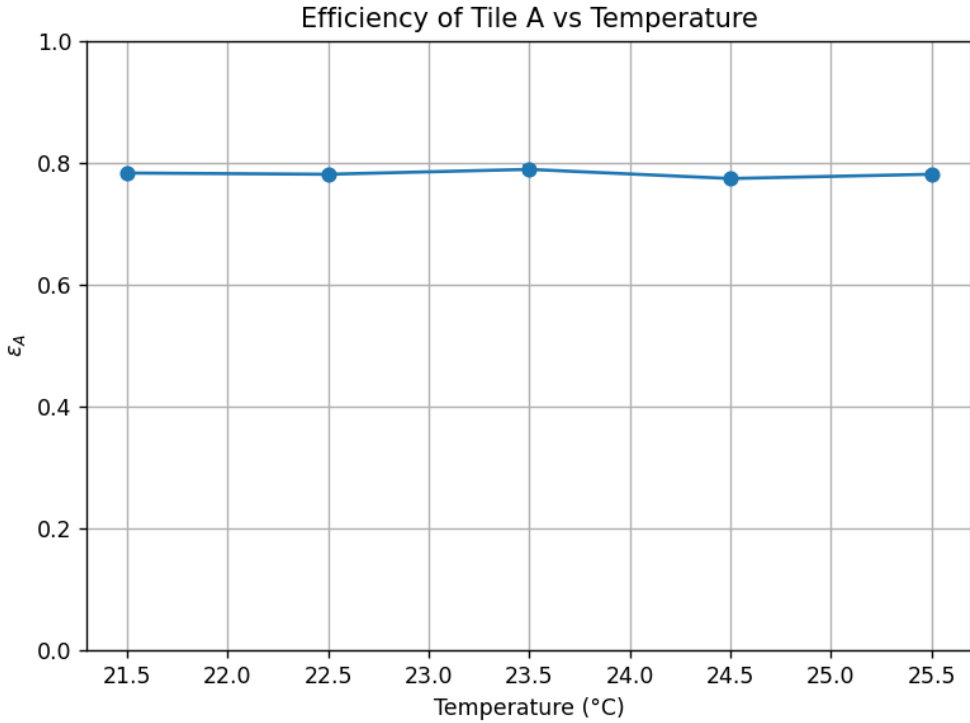


Figure 2.16: Efficiency of Tile A as a function of temperature. Errors are plotted but are small to be visualized at the scale.

The above plot summarizes the net changes in the detection efficiency at different temperature bins. In this study, we have considered a temperature bin spanning $1^{\circ}C$, however practically, with a more advanced detection unit, characterization can be performed for even smaller bin widths.

Efficiency of Tile B

By following a similar procedure as outlined for tile A, we characterize tile B also. For tile B, we collect ABC and AC coincidence readings and the efficiency of Tile B is given by:

$$\epsilon_B = \frac{N(ABC, T)}{N(AC, T)}$$

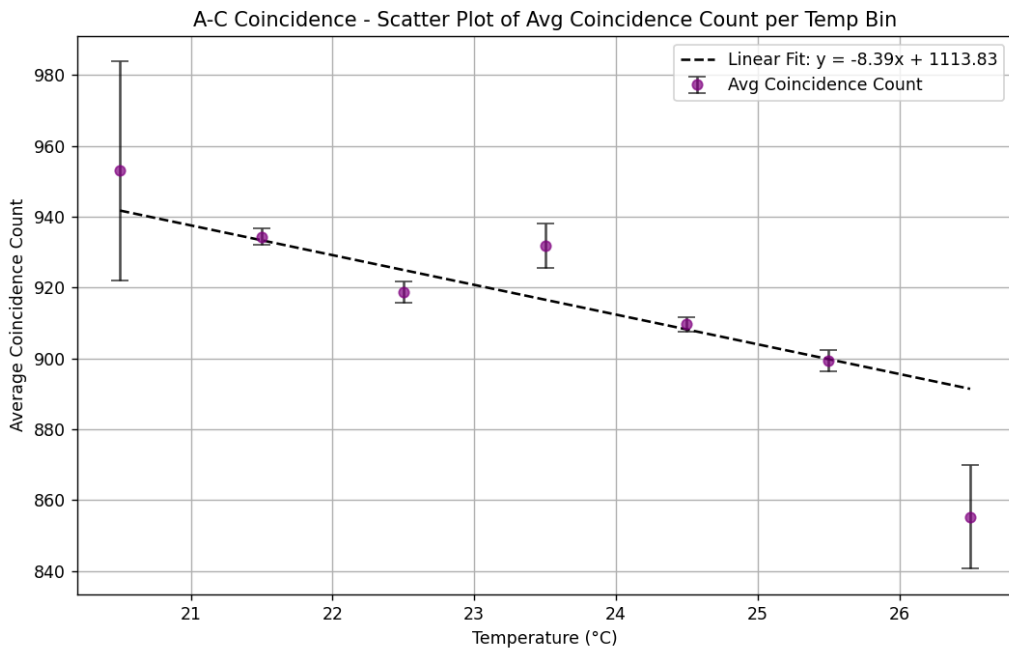


Figure 2.17: Average AC coincidence counts across temperature bins.

Temperature (°C)	ABC Count	AC Count	ϵ_B	$\delta\epsilon_B$
21–22	889.65 ± 2.47	934.36 ± 2.29	0.952	0.004
22–23	870.49 ± 3.36	918.65 ± 3.03	0.948	0.005
23–24	875.07 ± 5.15	931.87 ± 6.37	0.939	0.009
24–25	852.27 ± 1.90	909.60 ± 2.11	0.937	0.003
25–26	849.17 ± 3.22	899.40 ± 2.99	0.944	0.005

Table 2.2: Efficiency of Tile B (ϵ_B) and its uncertainty across temperature bins. Efficiencies are rounded to three decimal places.

Trend points to reducing average AC coincidence count as expected. AC coincidence counts across all temperature bins are significantly smaller than CB and AB coincidence counts. Since, in theory, all the three detection tiles are identical, such a large offset is not expected for any combination of two tiles. However, practically this is possible

due to SiPM and front end electronics performance. Slight variations in the physical arrangement, orientation and position of the setup can induce errors which can grow over time. Since these readings are taken over 586 detection cycles of 10 minutes each, we attribute this offset to instrumental errors induced due to detector performance with temperature correlations and human errors.

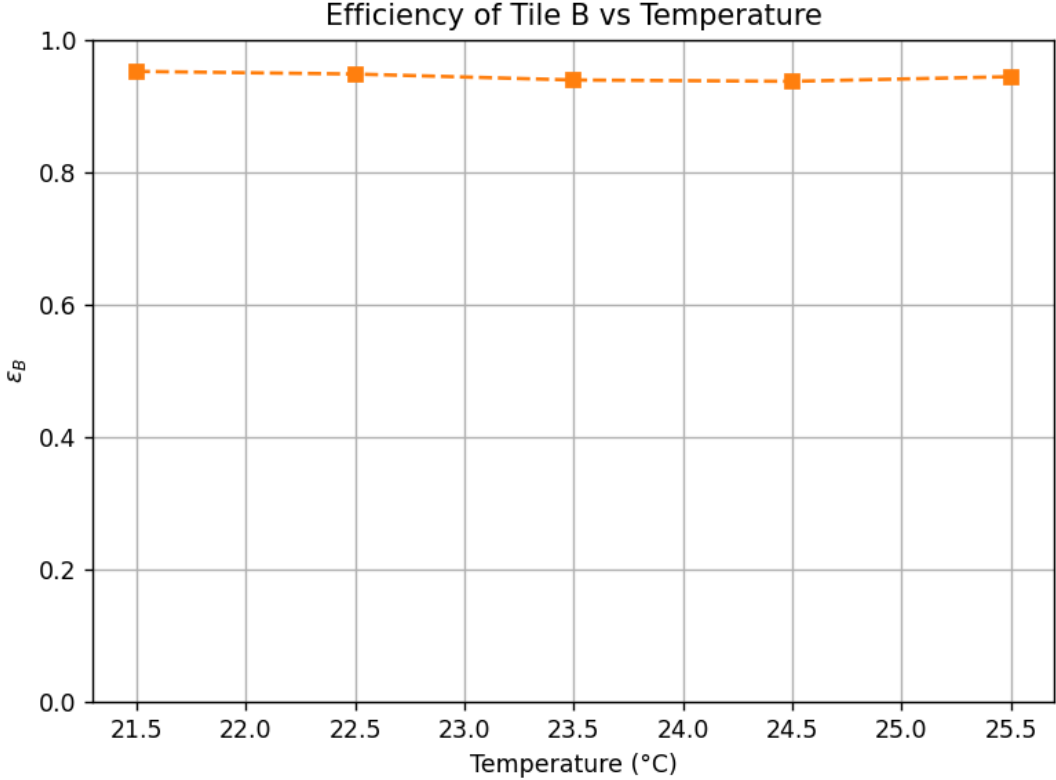


Figure 2.18: Efficiency of Tile B as a function of temperature. Errors are plotted but are small to be visualized at the scale.

The efficiency of tile B slightly drops as the temperature increases. For this case also, the final temperature bin has a sudden jump in efficiency due to same reasons mentioned above.

Efficiency of Tile C

By reiterating the aforementioned procedure, efficiency of Tile C is given by:

$$\epsilon_C = \frac{N(ABC, T)}{N(AB, T)}$$

Average AB coincidence also shows similar characterization to BC and AC coincidence. AB coincidence counts are significantly larger than average AC counts and comparable to average CB counts.

Temperature ($^{\circ}\text{C}$)	ABC Count	AB Count	ϵ_C	$\delta\epsilon_C$
21–22	889.65 ± 2.47	1215.30 ± 7.27	0.732	0.005
22–23	870.49 ± 3.36	1208.16 ± 2.64	0.721	0.003
23–24	875.07 ± 5.15	1197.46 ± 6.79	0.731	0.006
24–25	852.27 ± 1.90	1187.52 ± 6.89	0.718	0.004
25–26	849.17 ± 3.22	1182.94 ± 2.10	0.718	0.003

Table 2.3: Efficiency of Tile C (ϵ_C) and its uncertainty across temperature bins.

Efficiency of tile C is comparable to A but significantly lesser than B. Due to temperature variations, ABC coincidence and AB coincidence both reduce. This is due to detector efficiency reduction with temperature as discussed previously. Globally, a slight dip can be observed in tile C efficiency at higher temperatures as well but on an average there are slight fluctuations across.

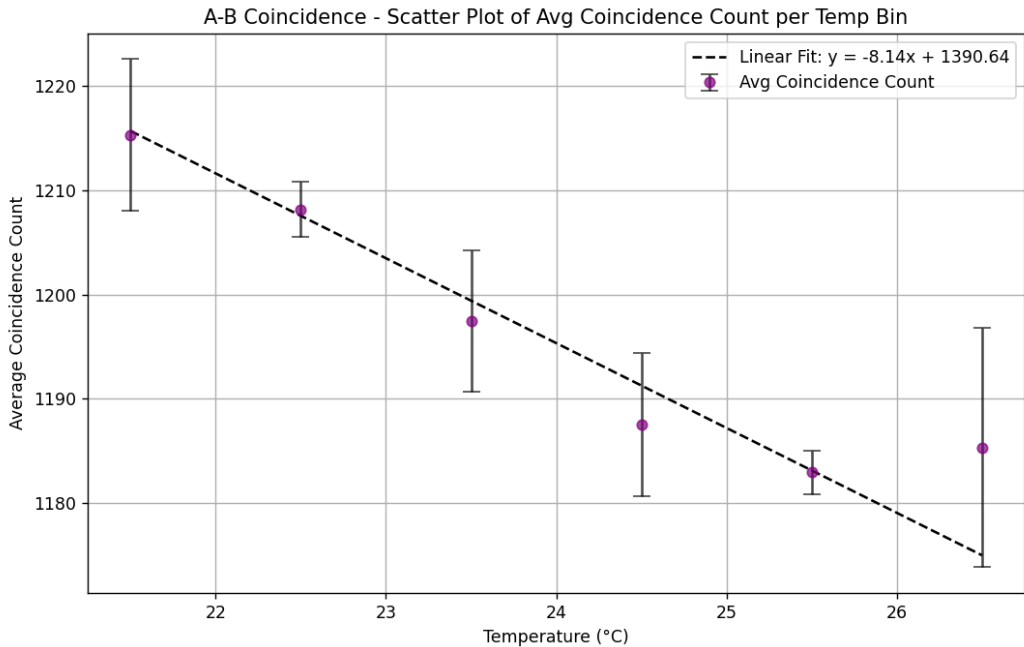


Figure 2.19: Average AB coincidence counts across temperature bins.

Compared to average CB and average AC coincidence counts, a much more visible trend is observed for AB coincidence. Across a temperature variation of 4°C . average AB coincidence count reduces by nearly 30 muons. This effect though not considerable at this scale can significantly amplify over more number of detection cycles as well as longer cycles. This experiment is conducted for detection cycles of 10 minutes each and a total of 586 cycles. This effect of average count reduction is already profound over these many detection cycles. As for tile A and tile B, for this tile also, the temperature bin of $26^{\circ}\text{C} - 27^{\circ}\text{C}$ is a curious case. The sudden jump in the average coincidence count is a result of significantly lesser number of readings in that temperature bin as compared to other temperature bins. Due to this the averaged value comes out to be larger than the count in the previous bin, thus defying the trend.

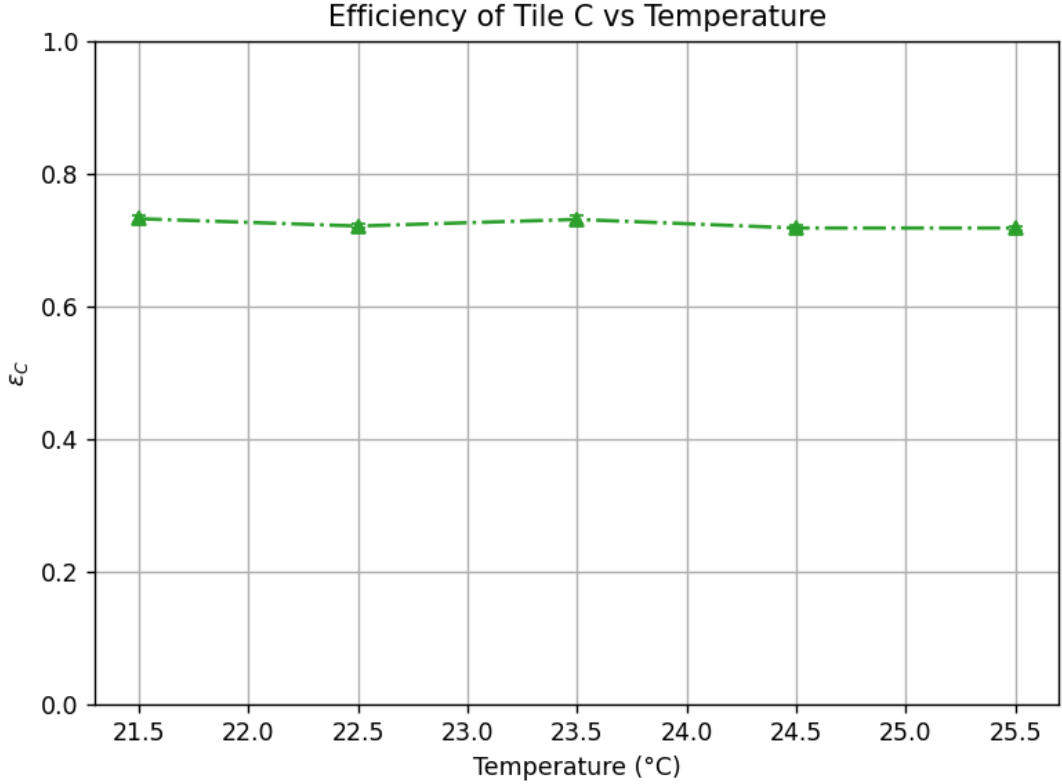


Figure 2.20: Efficiency of Tile C as a function of temperature. Errors are plotted but are small to be visualized at the scale.

Comparison of Tile Efficiencies

Since the experiment involves use of three and two detection tiles based upon the variation, it is important to understand Gross efficiency of the setup along with individual detection tile efficiencies. Gross efficiency is defined simply as;

$$\epsilon_{\text{gross}} = \epsilon_A \times \epsilon_B \times \epsilon_C$$

Due to relatively lower efficiencies of tile A and tile C, net efficiency of the setup reduces. Given below is the summary of detection efficiencies of tiles and the gross efficiency.

Temperature (°C)	$\epsilon_A \pm \delta\epsilon_A$	$\epsilon_B \pm \delta\epsilon_B$	$\epsilon_C \pm \delta\epsilon_C$	$\epsilon_{\text{gross}} \pm \delta\epsilon_{\text{gross}}$
21–22	0.783 ± 0.002	0.952 ± 0.004	0.732 ± 0.005	0.546 ± 0.004
22–23	0.781 ± 0.004	0.948 ± 0.005	0.721 ± 0.003	0.533 ± 0.005
23–24	0.789 ± 0.007	0.939 ± 0.009	0.731 ± 0.006	0.541 ± 0.008
24–25	0.774 ± 0.002	0.937 ± 0.003	0.718 ± 0.004	0.520 ± 0.004
25–26	0.781 ± 0.004	0.944 ± 0.005	0.718 ± 0.003	0.530 ± 0.005

Table 2.4: Comparison of efficiencies ϵ_A , ϵ_B , and ϵ_C across temperature bins, along with gross efficiency (ϵ_{gross}).

Tile B is seen to have the highest efficiency. Efficiencies of tile A and tile C are close by and relatively lesser than the tile B efficiency. As mentioned in previous sections, this is likely due to smaller signal-noise ratio for these tiles. The detection efficiencies largely

depend upon proper functioning of the front end electronics used in the scintillation tiles and their coupling to SiPMs. These varying detector efficiencies do affect the experimental readings and have to be corrected for to get accurate results.

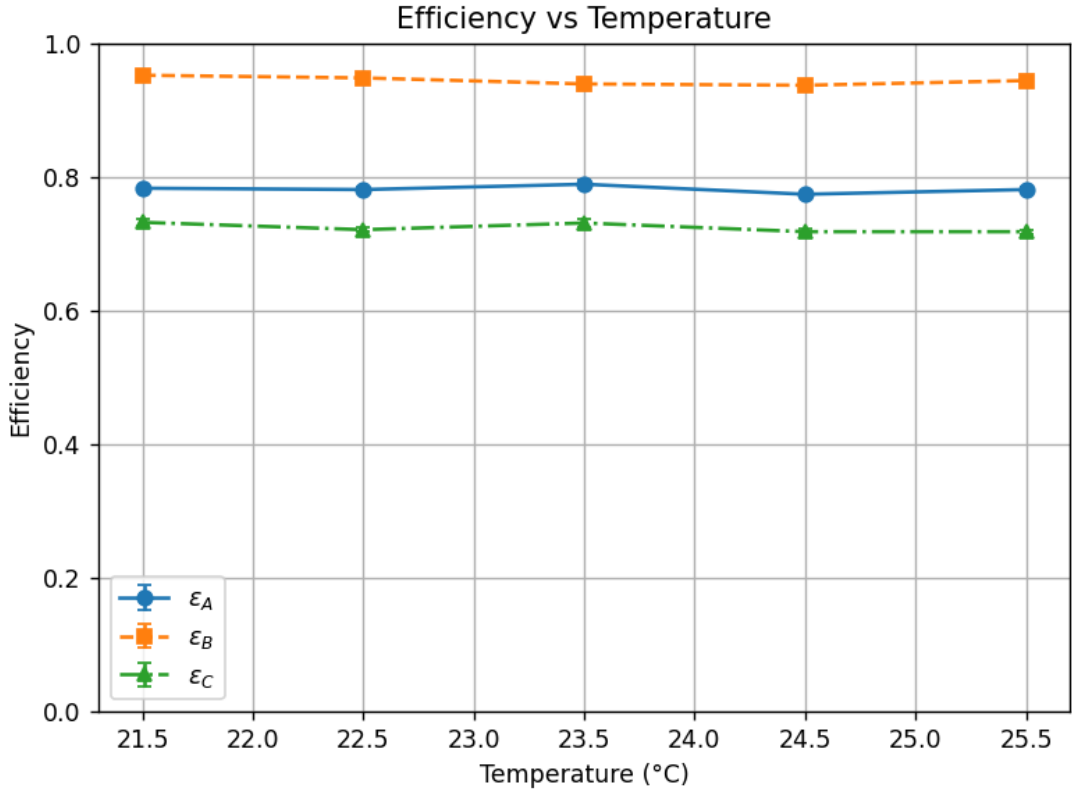


Figure 2.21: Comparison of tile efficiencies as a function of temperature.

A simulation in such a case provides a full-proof way of carrying out such experiments without the influence of external factors. In a simulation setup, all the plastic scintillators have the same 100 % detection efficiency. To mimic the experimental setting, a more advanced simulation would be required with detector efficiencies as a function of temperature.

2.3.3 Experimental Trials with Concrete target

This experimental procedure aims at understanding muon scattering through fiber integrated concrete slabs provided by the civil engineering department. The setup employed is shown in figure 3. In this experiment, we place concrete slabs between detector A and detectors B,C to determine flux attenuation of muons as they pass through the concrete slab. Muons are first recorded at detector A. From there they are incident on the target subsequently passing through detectors B and C. We record ABC coincidence over a range of temperature to determine the attenuation effect. This trial 1 lasted for 889 detection cycles with each detection cycle being 10 minutes long.

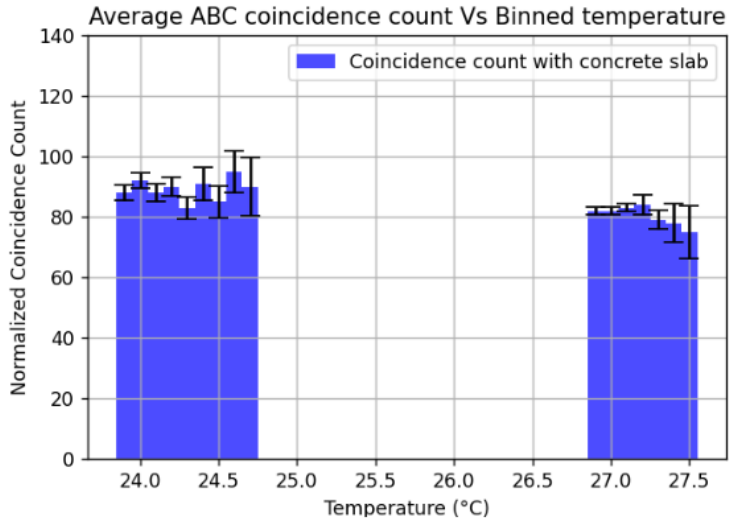


Figure 2.22: Plot shows average ABC coincidence count with concrete slab acting as the target. The count is recorded for multiple temperature bins separated by $0.10^{\circ}C$.

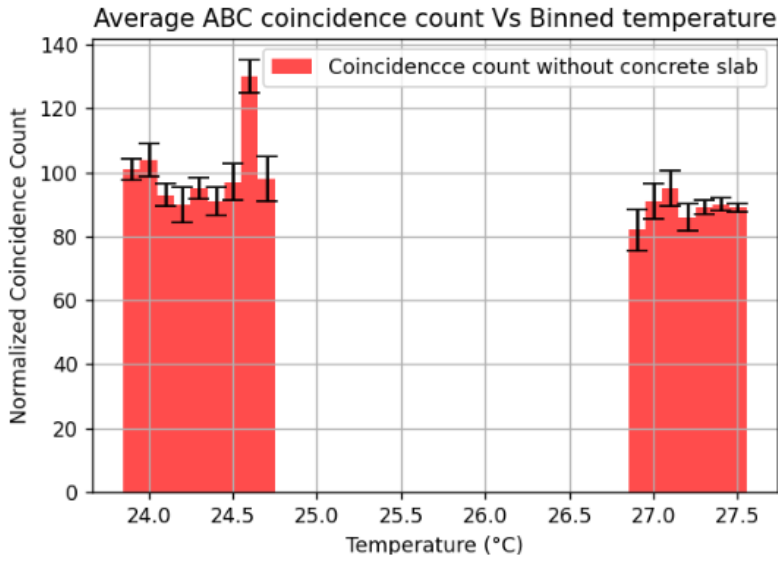


Figure 2.23: Plot shows average ABC coincidence count without concrete slab between detector A and detectors B,C. The count is recorded for multiple temperature bins separated by $0.10^{\circ}C$.

Figures show the average triple coincidence count for each binned temperature of range $0.10^{\circ}C$. By binning the temperature so close by, it is made sure that the efficiency variation of detection with temperature is effectively accounted for. General trend still points to the fact that at higher temperature bins, the average coincidence count is lesser than at lower temperature bins accounting for reduced efficiency of detection.

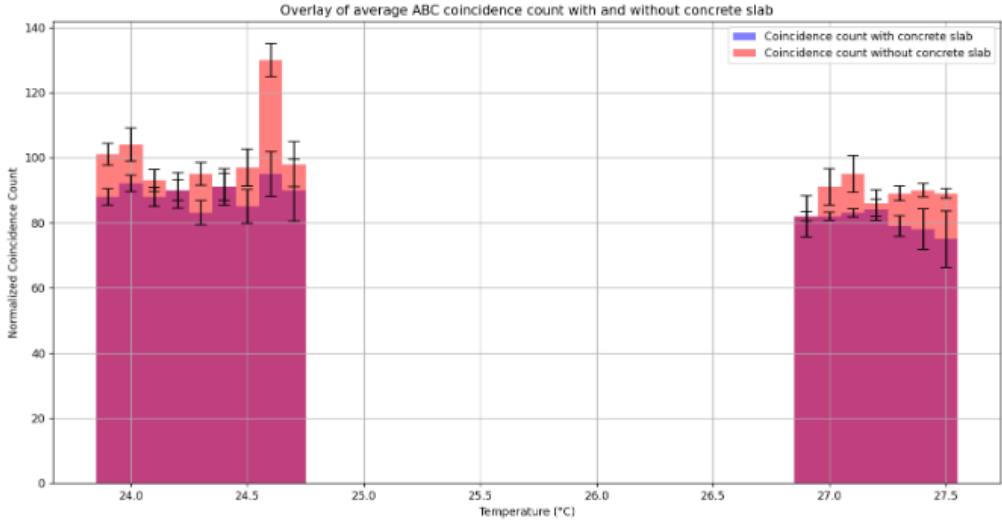


Figure 2.24: Overlaid plot for average ABC coincidence count with and without concrete target. Red histogram represents average coincidence count with target and blue histogram is for without target readings.

The overlaid plot shown in the figure above provides valuable information on comparison of average triple coincidence counts with and without the obstruction of concrete slabs. Global trend across temperature bins clearly shows that the average muon count is higher when no obstruction is placed in the path. On introducing concrete target, there is notable reduction in the average muon count.

Trial 2 of the same experiment was performed, which lasted for 2 hours. The data consists of 1 hour of readings without a concrete target and 1 hour of readings with a concrete target.

- ABC coincidence count
- Without concrete slab: 561 ± 24
- With concrete slab: 462 ± 21

With a smaller duration of experimental run, we altogether eliminate the effect of temperature variations. This ensures that the detectors are operating at their natural detection efficiencies at particular temperature. Minor temperature variations can be safely neglected. This trial also confirms that the muon scattering is taking place through the concrete slab leading to smaller coincidence counts.

These experimental verifications are also tested with simulation results.

2.4 Geant4 simulation setup for MST

2.4.1 Concrete target in Geant4

I present the simulation results obtained for cement block of thickness 10 cm, 15 cm, 18.3 cm and 25 cm. Cement block of thickness 18.3 cm matches with the experimental setup and the other two thicknesses are chosen for comparison purpose.

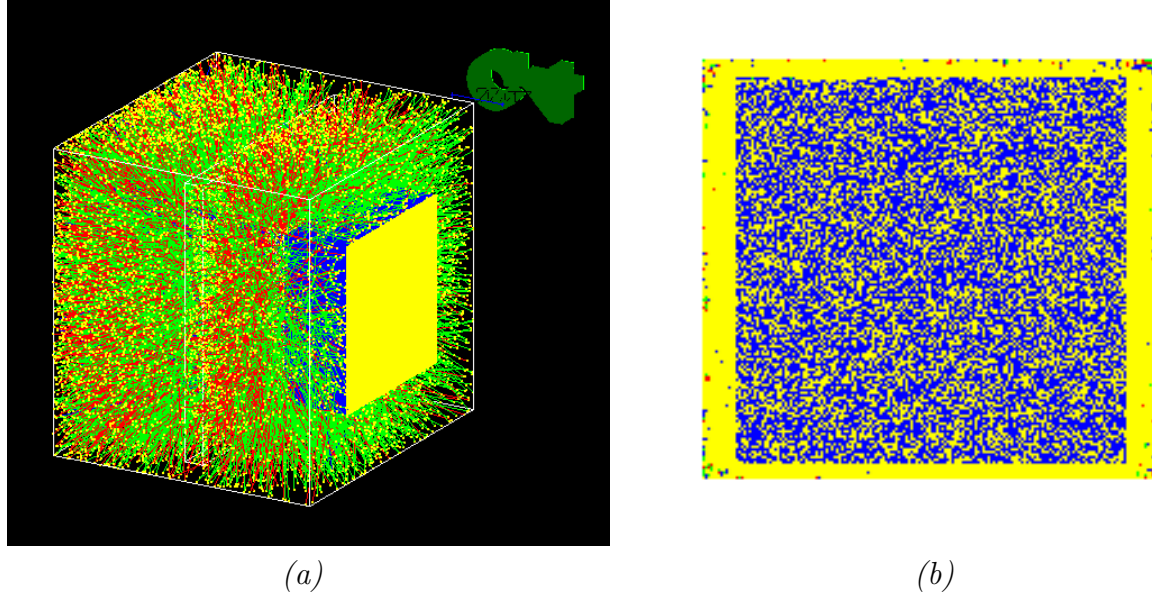


Figure 2.25: Panel (a) shows the 1,00,000 run simulation for a 10 cm thick concrete slab. Panel (b) shows the scattered pattern on the screen (yellow) with source geometry superimposed (central blue planar region).

I run a simulation with 1,00,000 muons incident on the setup and study the muon hits at each detector and energy depositions.

Table 2.5: Muon counts for concrete slab without hole (100,000 muons run)

Slab Thickness (cm)	B1	B2	T2	T1
10	96969	96410	99987	99933
15	96313	95596	99989	99924
18.8	96097	95239	99990	99933
25	95172	94133	99985	99925

Since the setup consists of four scintillation detectors, B1 and B2 refers to the bottom two detectors i.e detectors post the target and T1, T2 refer to the top two detectors on which muons are incident directly from the source before they interact with the target. Hence, as expected top two detectors have muon counts very close to 1,00,000. Since muons have energy spectrum and they interact in a certain way with the detectors also, depositing their energies into them, the minor count imbalance is understood. The mean scattering angle is directly proportional to the thickness and Z of the target. Concrete is a composite material composed primarily of cement, aggregates (such as sand and gravel), and water. Its effective atomic number (Z_{eff}) is not a fixed value but rather a weighted average that depends on the elemental composition of its constituents. Typically, Z_{eff} for concrete lies in the range of 11 to 13 [24]. The effective atomic number is critical in determining concrete's interaction with high-energy particles such as cosmic muons.

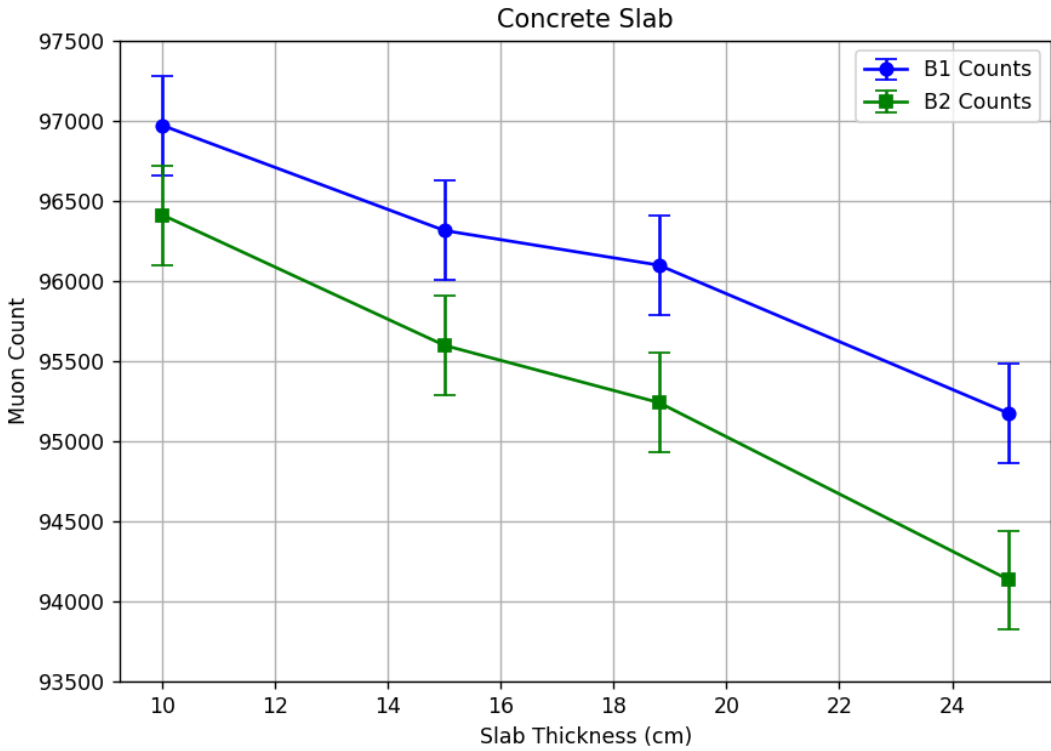


Figure 2.26: Figure shows B1 and B2 detector counts for concrete target (slab) with varying thickness

As expected the muon count recorded at both the bottom detectors reduces with increasing thickness of the concrete slab. The count in B2 detector is lesser than B1 for two primary reasons:

- Since B1 and B2 are separated by 1 cm and each detector is 3 cm thick, some muons might be scattered at angles such that they pass through the B1 detector but miss the B2 detector and hence are not counted.
- Since muons are depositing energies in detectors as well as target, with increasing thickness of target, more energy is deposited and due to limited lifespan of these muons, they might not be reaching B2 detector.

Overall trend confirms that with the aid of MST, one can characterize materials based on their constituents and dimensions. This is a primary result facilitating more advanced analysis with defects.

2.4.2 Lead target in Geant4

Similar detector count measuring simulation exercise is carried out for Lead block with varying thickness of 5 cm, 7 cm, 9 cm and 11 cm.

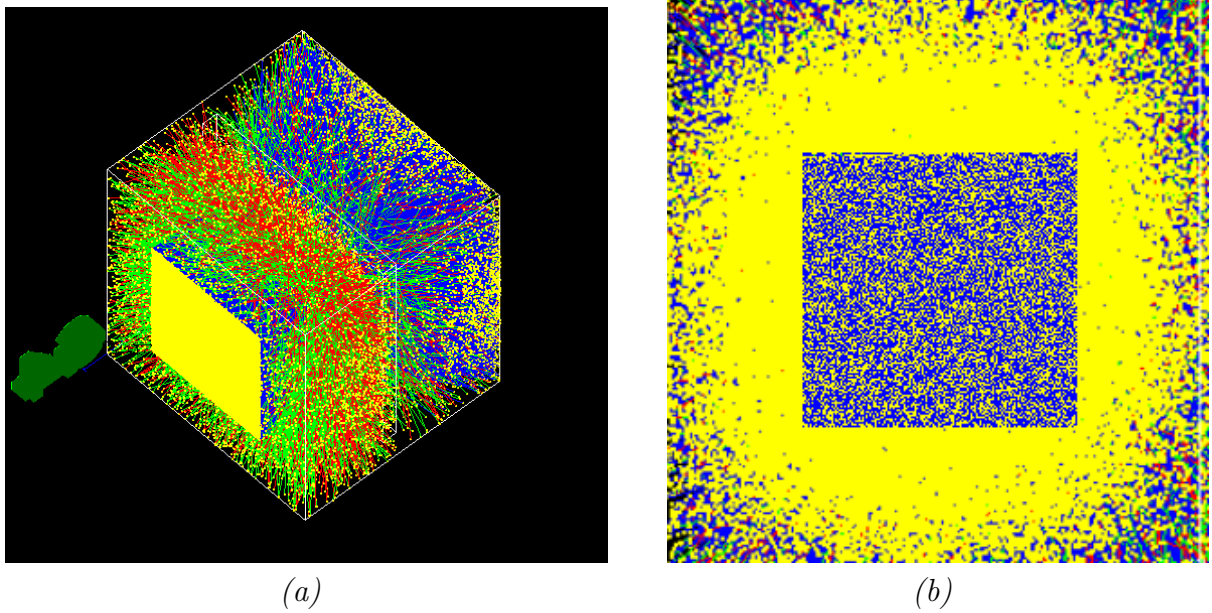


Figure 2.27: Panel (a) shows the 1,00,000 run simulation for a 7 cm thick lead slab. Panel (b) shows the scattered pattern on the screen (yellow) with source geometry superimposed (central blue planar region).

Lead has an atomic number of $Z = 82$ and a very small radiation length due to high Z . The radiation length X_0 is a fundamental property of a material that characterizes the mean distance over which a high-energy electron loses all but $1/e$ of its energy via bremsstrahlung. It also represents $7/9$ of the mean free path for pair production by high-energy photons. An approximate empirical formula for calculating the radiation length in units of g/cm^2 is given by [26]:

$$X_0 \approx \frac{716.4 A}{Z(Z + 1) \ln(287/\sqrt{Z})}$$

where Z is the atomic number and A is the atomic mass of the material. For lead ($Z = 82$, $A = 207.2$), the radiation length is approximately $6.37 \text{ g}/\text{cm}^2$, which corresponds to a physical length of about 0.5612 cm considering lead's density of $11.35 \text{ g}/\text{cm}^3$. This relatively short radiation length makes lead an effective material for shielding against electromagnetic radiation. As described previously, the mean scattering angle is directly proportional to Z and inversely proportional to X_0 . Hence lead offers a lot more scattering as compared to the concrete target. This is very clearly seen from the scattering pattern on the screen in comparison to the concrete scattering pattern.

Results for lead target with varying thickness are presented below:

Table 2.6: Muon count for Lead slab without hole (100,000 muons run)

Slab Thickness (cm)	B1	B2	T2	T1
5	90145	87940	99983	99938
7	86895	84089	99985	99952
9	82124	77958	99991	99940
11	75689	71564	99989	99925

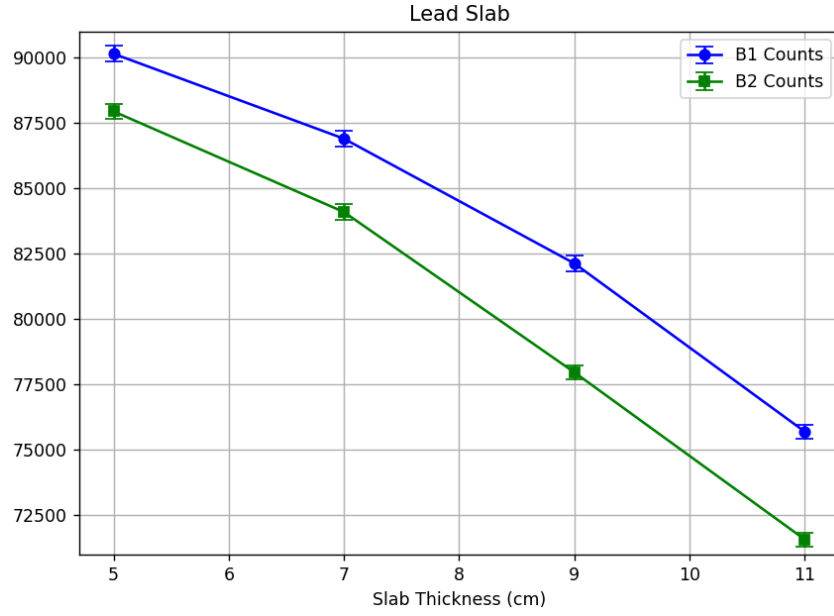


Figure 2.28: Figure shows B1 and B2 detector counts for lead target (slab) with varying thickness

2.4.3 Lead slab with complete hole defect in Geant4

In this section, I have presented results for a complete holed lead slab (complete defect) for 7 cm and 9 cm thick lead slab. As mentioned, we consider 9 different hole radii varying from 10 cm to 50 cm. The results show a conclusive trend in the increasing muons flux with increasing hole radius.

Lead slab thickness: 7 cm					Lead slab thickness: 9 cm				
Hole radius	B1	B2	T2	T1	Hole radius	B1	B2	T2	T1
10 cm	18320	17737	20000	19993	10 cm	17649	16773	19998	19987
15 cm	18303	17720	19993	19985	15 cm	17706	16887	19998	19998
20 cm	18283	17719	19993	19989	20 cm	17664	16893	19999	19987
25 cm	18242	17743	19997	19988	25 cm	17903	17278	19990	19982
30 cm	18834	18594	19993	19977	30 cm	18670	18384	19996	19987
35 cm	19366	19229	19999	19983	35 cm	19285	19156	19997	19979
40 cm	19698	19656	19999	19986	40 cm	19673	19633	19997	19984
50 cm	19743	19703	19995	19991	50 cm	19733	19692	19996	19991

Table 2.7: Comparison of detector counts (T1,T2,B1 and B2) for lead slab thicknesses of 7 cm and 9 cm at different hole radii.

Significantly less number of detector counts are seen for lead slab of thickness 9 cm as compared to 7 cm. With the increasing hole radius, i.e a bigger defect, more muons pass through unobstructed and the same is observed from the readings.

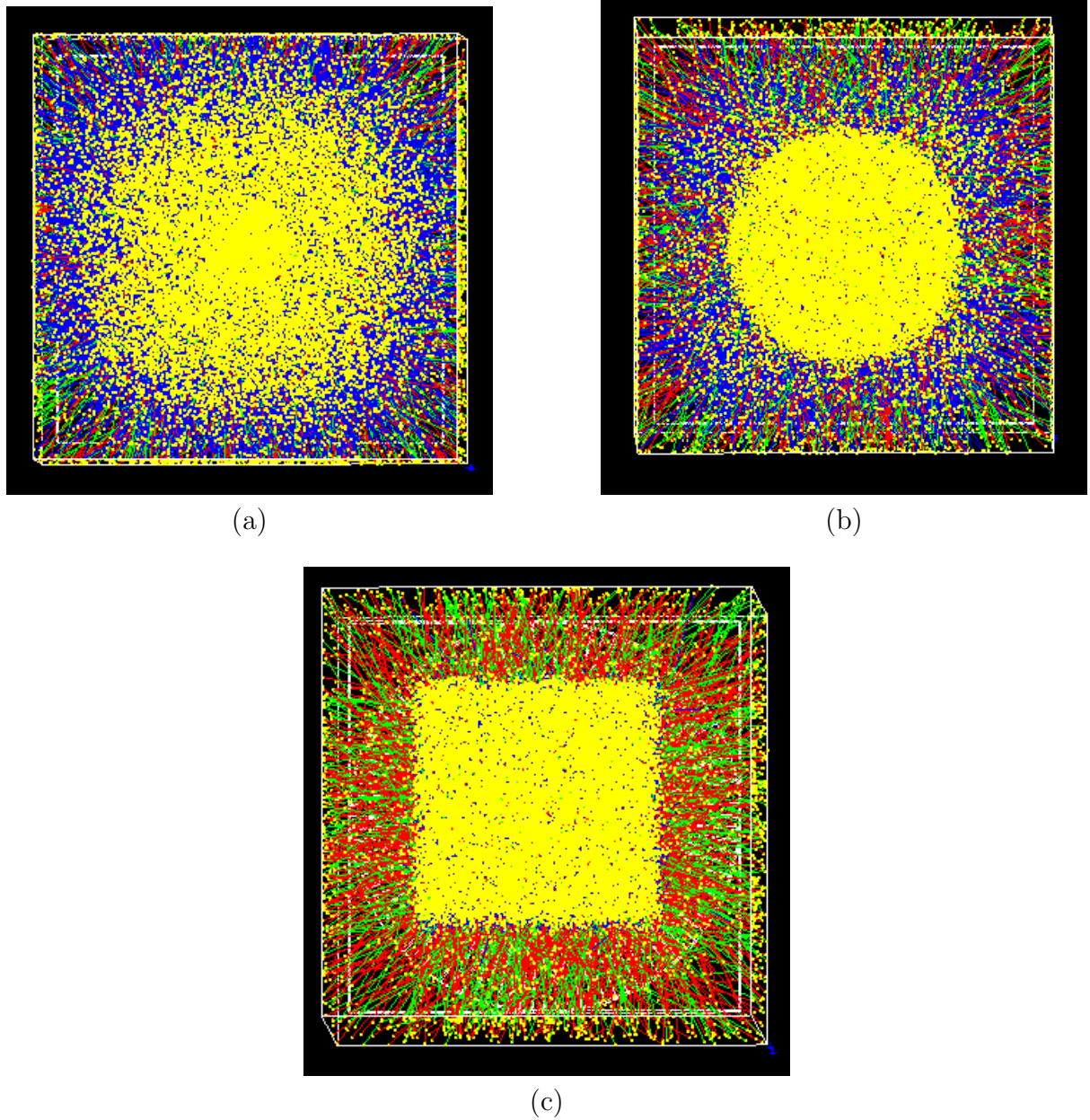
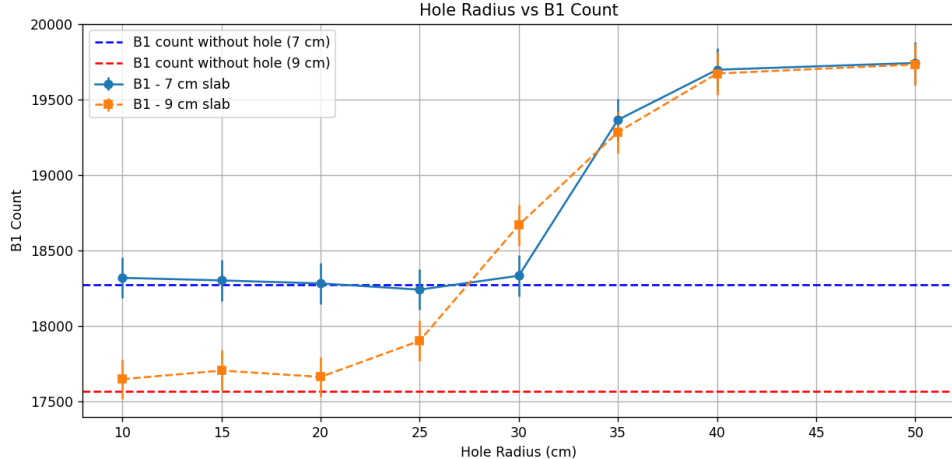
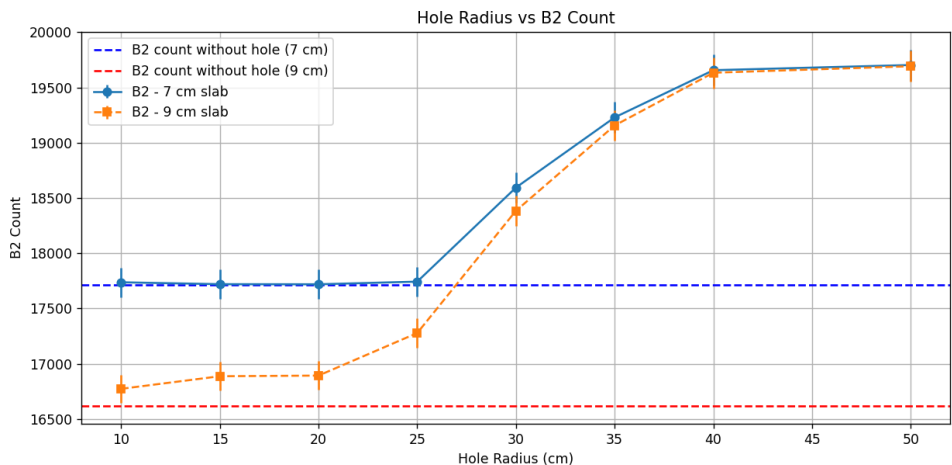


Figure 2.29: Comparison of scattering patterns as observed on the screen for lead slab of 7 cm with central hole radius (a) 10 cm, (b) 30 cm, and (c) 50 cm. The 10 cm hole scattering pattern is challenging to map onto the defect. However the 30 cm hole features a circular pattern on the screen clearly giving the image of the defect itself. A 50 cm hole exceeds the dimensions of the source geometry and hence the source is mapped onto the screen. These provide critical insights into the mapping of the scattering pattern on the screen to the defect in the target.

With the obtained results, we perform comparison between the B1 (Bottom detector 1) and B2 (Bottom detector 2) counts of muons with a reference of the B1 and B2 counts for no defect geometry (refer sections 4.1 and 4.2 for the results). For a 7 cm thick lead slab, the reference count thus is 86895 for B1 and 84089 for B2. For a 9 cm thick lead slab, the reference count is 82124 for B1 and 77958 for B2.



(a)



(b)

Figure 2.30: Plots show muon counts with changing complete hole defect radius for 7 cm and 9 cm thick lead slabs for B1 and B2 detectors. Blue and red dotted lines respectively represent the reference counts for 7 cm and 9 cm thickness of lead slab. Blue solid line is B1/B2 counts for 7 cm thick lead slab and orange solid line is B1/B2 counts for 9 cm thick lead slab.

These simulations provide conclusive results on the muon counts at B1 and B2 detectors with changing hole radius. As expected, muon counts significantly increase as the hole radius is increased. Beyond hole radius of 20 cm, there is a significant increase in the detection count. This is due to more muons passing through the target unobstructed. Muon count is fairly close to the reference line for smaller complete defect radii but is highly distinguishable from the reference line for larger defects. Similar trend is observed for B1 and B2 indicating consistency of results. This provides a conclusive evidence that given a reference point, complete defects in high-Z targets can be readily detected with muon scattering techniques. From the scattering patterns diagrams it is seen that, if defects are of a certain threshold size, they can be mapped onto the screen as well.

2.4.4 Lead slab with partial hole defect in Geant4

In this section, I present results for a partial holed lead slab (partial defect) of 7 cm thickness. Partial holes of thickness 6 cm and 5 cm are considered. For this case also, we consider 9 different hole radii varying from 10 cm to 50 cm. The results show a conclusive trend in the increasing muons flux with increasing hole radius.

Table 2.8: Muon counts for 7 cm lead slab thickness with **6 cm hole thickness** across varying hole radii.

Slab Thickness	Hole Radius	B1	B2	T2	T1
7 cm	10 cm	18303	17689	19993	19978
	15 cm	18252	17663	19994	19983
	20 cm	18285	17734	19993	19983
	25 cm	18325	17863	19999	19982
	30 cm	18749	18491	19999	19990
	35 cm	19159	18953	19995	19982
	40 cm	19320	19146	20000	19992
	50 cm	19422	19250	19999	19989

Table 2.9: Muon counts for 7 cm lead slab thickness with **5 cm hole thickness** across varying hole radii.

Slab Thickness	Hole Radius	B1	B2	T2	T1
7 cm	10 cm	18262	17660	19998	19992
	15 cm	18314	17700	19996	19986
	20 cm	18259	17700	20000	19992
	25 cm	18357	17833	19998	19992
	30 cm	18727	18398	19996	19990
	35 cm	18966	18690	19999	19988
	40 cm	19199	18956	19999	19987
	50 cm	19162	18899	19998	19986

Since the partial hole defect resides inside the target and is not visible on the outside, the scattering pattern from this kind of defect provides crucial information about mapping of the target volume. It is expected that for such a partial defect, the scattering pattern would be more smeared as compared to the complete defect. This is since the muons have to pass through a larger volume of target as compared to the complete defect scenario and hence will observe more scattering along the way. Deeper the defect lies in the target, more smeared image would be formed on the screen. Thus, hole of thickness 6 cm for a 7 cm thick lead slab will give us clearer images of the defect if detectable. This is demonstrated below.

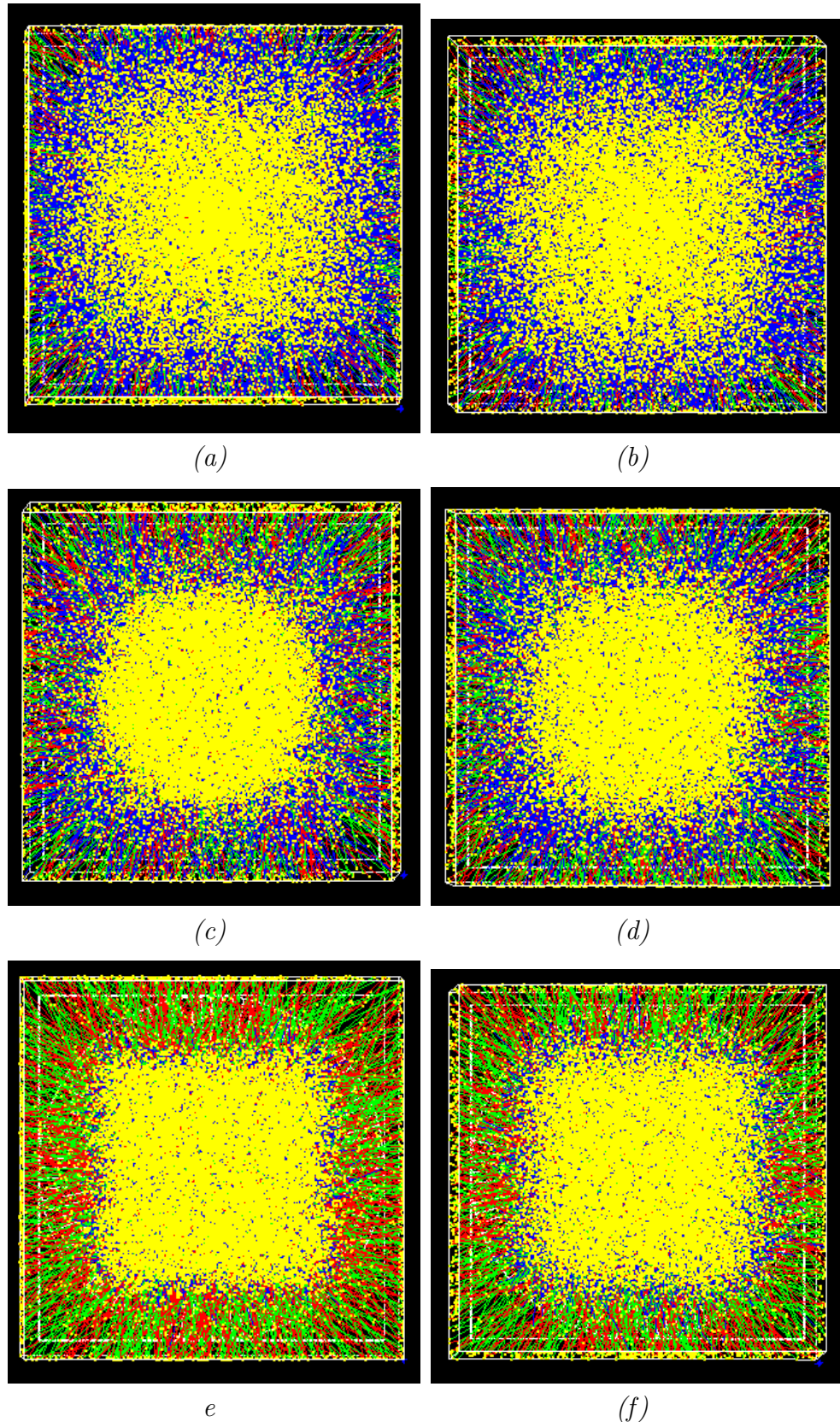


Figure 2.31: The left panel shows the scattering pattern observed for a partial hole of 6 cm thickness and the right one shows pattern for hole of 5 cm thickness. Figures (a),(c) and (d) are scattering patterns for 6 cm thick partial hole with hole radii 10 cm, 30 cm and 50 cm respectively. Figures (b),(d) and (f) are scattering patterns for 5 cm thick partial hole with hole radii 10 cm, 30 cm and 50 cm respectively.

As can be observed from the scattering patterns above, there is slightly more smirked pattern for the partial hole of lesser thickness. This as mentioned is expected since muons have to travel a larger solid volume of the target material in that case. The 30 cm hole partial defect is still mapped onto the screen irrespective of more smirking compared to the complete hole case. As mentioned earlier, since the 50 cm hole radius significantly exceeds dimensions of the source geometry, the source geometry is directly mapped on the screen in both the cases. Analysis of scattering pattern from 10 cm hole radius is not evidence and may require pixeleted detector setup to make conclusions about the mapping of such small defects.

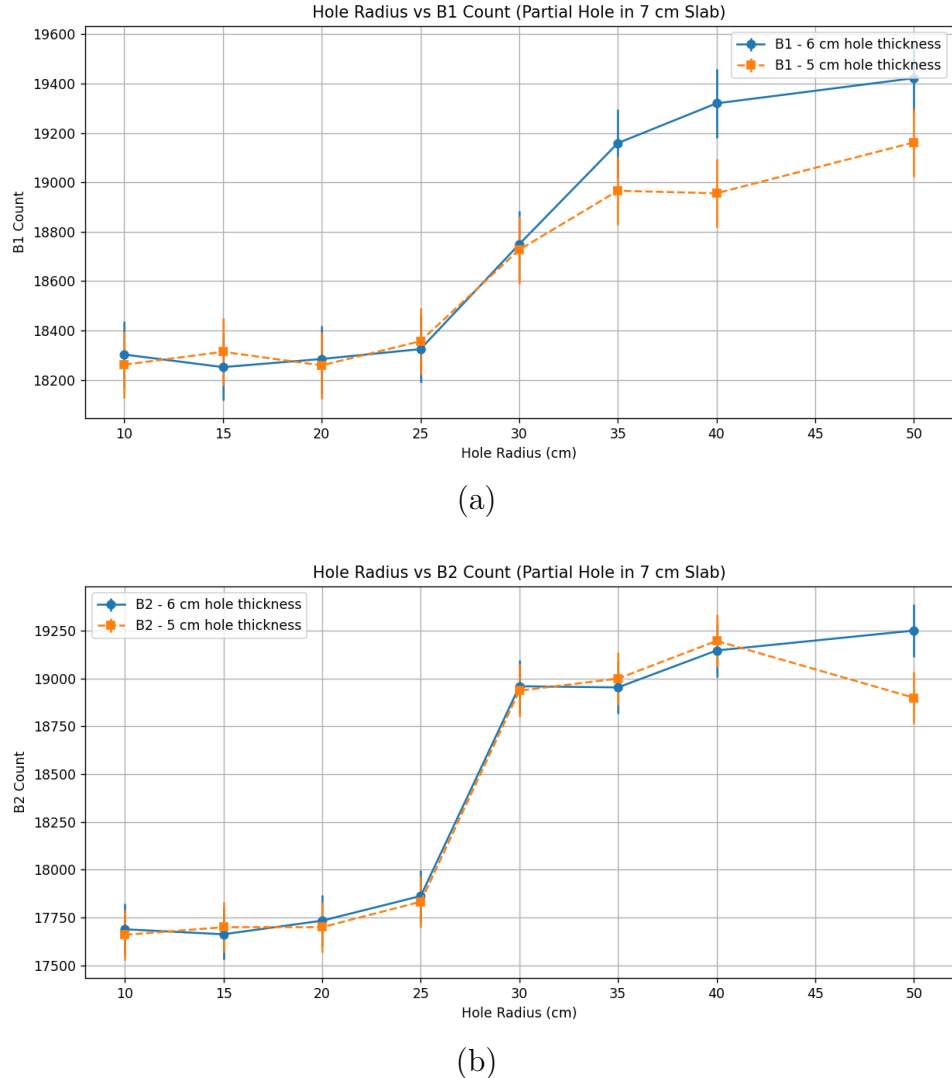


Figure 2.32: Plots show muon counts with varying partial hole defect radius for 6 cm and 5 cm thick defects in a 7 cm thick lead slab for B1 and B2 detectors. For panel (a), blue solid line shows B1 counts for 6 cm thick defect and orange solid line shows B1 counts for 5 cm thick defect. Same convention is followed for panel (b) showing B2 counts.

2.5 Comparison plots for defect cases

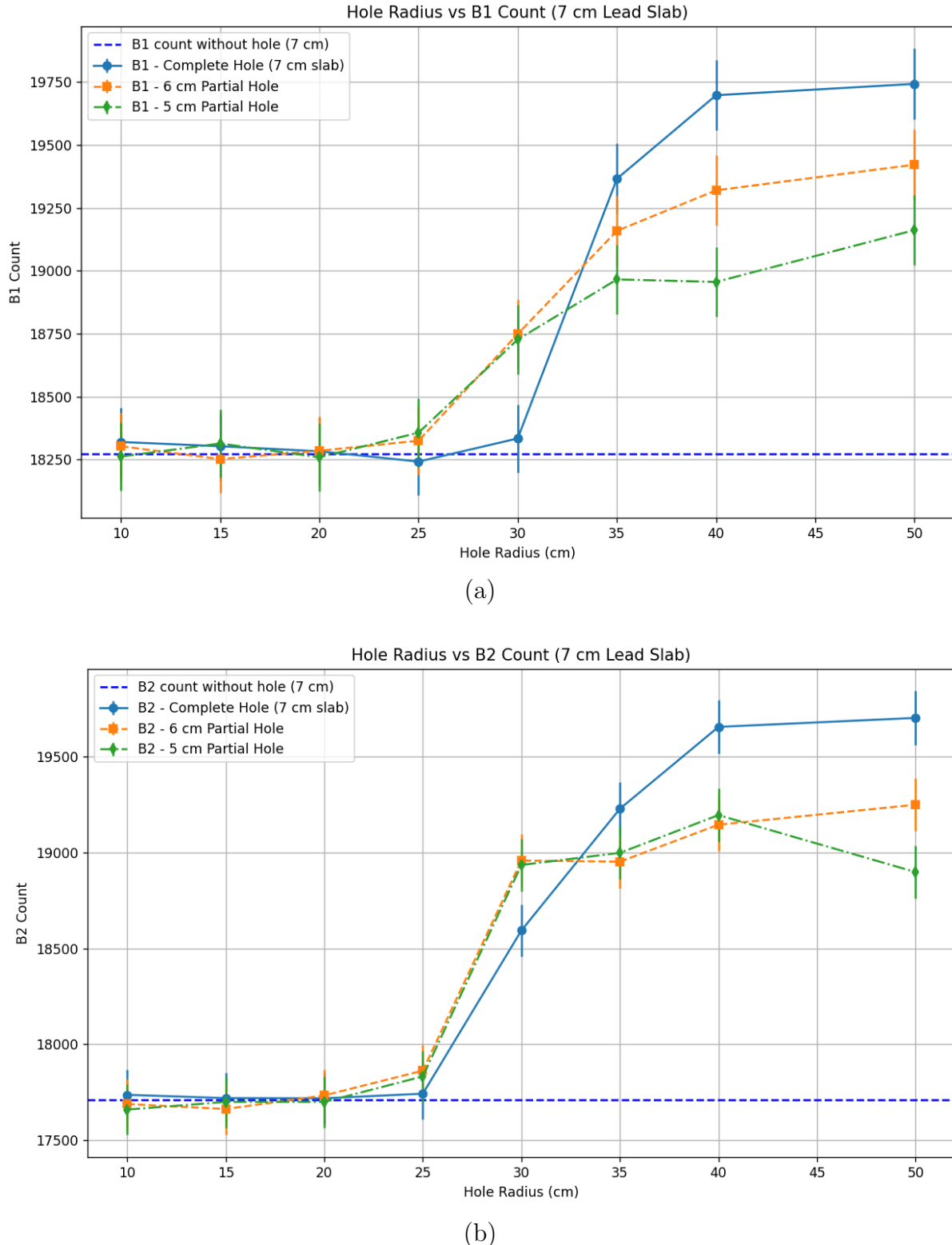


Figure 2.33: Plot shows combined results for muon counts at B1 detector (panel a) and B2 detector (panel b) for the no defect, complete defect and partial defect lead slab cases. Dotted blue lines are reference counts from no defect targets.

2.6 Discussion

This study has focused upon the experimental and simulation based demonstration of the usefulness and effectiveness of the muon scattering based tomography technique. Experimentally, by considering fiber reinforced concrete slabs, we successfully demonstrate the attenuation in the muon flux on introducing an obstructing target. This is demonstrated in two different experimental runs while carefully considering the temperature based variations in the detection efficiency of setup.

Followed by experimental verification, we have considered a simulation with a planar source of muons such that muons are incident perpendicular to the detectors and the target. The planar source helps generate a larger statistics and minimizes the intricacies related to the four detector coincidence. Simulating with actual spatial and temporal distribution of muons is also a possibility. However, that significantly increases the simulation time and provides lesser statistics. With angular distribution in consideration, achieving a four detector coincidence for very large number of muons is a significantly computationally expensive task.

With the four detector setup, we have demonstrated the muon flux attenuation for three different cases namely: target with no defect, target with a complete defect and target with a partial defect. Target with no defect shows the highest muon scattering and shows the highest muon flux attenuation as expected. We have mapped the muon scattering pattern onto the screen of the Geant4 world to better understand these effects. Target with a complete defect i.e holed lead slab with varying hole thickness, shows the least flux attenuation for holes of radius larger than 20 cm. Comparison between partially holed targets with different hole thicknesses provide critical insights into the defect mapping. There is a significant increase in the muon count at detectors B1 and B2 for holed and partially holed targets as compared to no defect target (blue dotted reference line).

Future prospects of this work include a detailed study of different defect types with the aid of experiments with pixelated detectors to map the internal volume of the target with high resolution. A real life simulation can be build with the use of CRY library that generates a realistic angular and energy distributions of cosmic muons. This will greatly aid in developing a field based movable device which can be used on the go to map the internal volumes of any small scale structure and determine defects in given samples. This method provides a solid ground for non destructive testing for small scale civil and other structures.

Bibliography

- [1] T. A. Moore, J. L. Harton, and D. Hagen, "A low-cost cloud chamber for radiation detection: A hands-on approach for teaching radiation physics," *American Journal of Physics*, vol. 86, no. 3, pp. 206–210, 2018.
- [2] J. A. Fernández and A. M. Calaf, "Visualization and analysis of cosmic ray muons using a cloud chamber," *Physics Education*, vol. 57, no. 2, p. 025015, 2022.
- [3] H. P. Robertson, "The Physics of Cloud Chambers: Theory and Applications," *Reviews of Modern Physics*, vol. 22, no. 3, 2015.
- [4] D. Griffiths, *Introduction to Elementary Particles*, 2nd ed., Wiley-VCH, 2008.
- [5] Harvard Science Demonstrations, "Cloud Chamber," Harvard University. Accessed November 3, 2024. Available: <https://sciencedemonstrations.fas.harvard.edu/presentations/cloud-chamber>.
- [6] P.A. Zyla et al. (Particle Data Group), "Review of Particle Physics," *Progress of Theoretical and Experimental Physics*, vol. 2020, no. 8, p. 083C01, 2020. Available: https://pdg.lbl.gov/2020/tables/contents_tables_mesons.html.
- [7] CAEN S.p.A., *SP5620CH – Cosmic Hunter: Educational Kit for Cosmic Ray Detection*, <https://www.caen.it/products/sp5620ch/>, accessed May 28, 2025.
- [8] M. Lagrange, *Introduction to Muography*, Working Experience Week, CERN Indico, 2024. <https://indico.cern.ch/event/1395474/contributions/5865876/>.
- [9] CMS Collaboration, *Muon Tomography*, CMS Experiment, CERN, 2024. <https://cms.cern/content/muon-tomography>.
- [10] Qun-Gang Wen, *Research on rapid imaging with cosmic ray muon scattering tomography*, Scientific Reports, vol. 13, Article number: 19718, 2023. <https://doi.org/10.1038/s41598-023-47023-w>.
- [11] L. Bonechi, R. D'Alessandro, and A. Giannanco, *Atmospheric muons as an imaging tool*, Reviews in Physics, vol. 5, 100038, 2020.
- [12] P. Stowell et al., *Figures of Merit for the Application of Muon Tomography to the Characterization of Nuclear Waste Drums-19253*, WM2019 Conference, Phoenix, Arizona, 2019.
- [13] C. Thomay et al., *Passive 3D imaging of nuclear waste containers with Muon Scattering Tomography*, Journal of Instrumentation, vol. 11, P03008, 2016.

- [14] S. Pesente *et al.*, *First results on material identification and imaging with a large-volume muon tomography prototype*, Nuclear Instruments and Methods in Physics Research A, vol. 604, pp. 738–746, 2009.
- [15] M. Stapleton *et al.*, *Angle Statistics Reconstruction: a robust reconstruction algorithm for Muon Scattering Tomography*, Journal of Instrumentation, vol. 9, P11019, 2014.
- [16] K. N. Borozdin *et al.*, *Image reconstruction and material Z discrimination via cosmic ray muon radiography*, Nuclear Instruments and Methods in Physics Research A, vol. 513, pp. 554–558, 2003.
- [17] H. K. M. Tanaka *et al.*, *Muography*, Nature Reviews Methods Primers, vol. 3, Article number: 88, 2023.
- [18] L. Oláh *et al.*, *Muography and its potential applications to mining and rock engineering*, Rock Mechanics and Rock Engineering, vol. 53, pp. 4893–4907, 2020.
- [19] J. Peña-Rodríguez, J. Jaimes-Teherán, K. Dlaikan-Castillo, and L. A. Núñez, *MUYSC: an end-to-end muography simulation toolbox*, Geophysical Journal International, vol. 237, no. 1, pp. 540–556, 2024.
- [20] G. Leone *et al.*, *Muography as a new complementary tool in monitoring volcanic hazard: implications for early warning systems*, Proceedings of the Royal Society A, vol. 477, no. 2253, 2021.
- [21] P. Martinez Ruiz-del Arbol, P. Gomez Garcia, C. Diez Gonzalez, and A. Orio-Alonso, *Non-destructive testing of industrial equipment using muon radiography*, Philosophical Transactions of the Royal Society A, vol. 377, no. 2137, 2018.
- [22] P. Martínez Ruiz del Árbol, *Muography as a Non-Destructive Testing Technique to Solve Problems in the Industry*, Presented at IFCA, 21 November 2019, <https://indico.ifca.es/event/1314/attachments/1007/1316/document.pdf>.
- [23] International Atomic Energy Agency, *Muon Imaging: How Cosmic Rays Help Us See Inside Pyramids and Volcanoes*, <https://www.iaea.org/newscenter/news/muon-imaging-how-cosmic-rays-help-us-see-inside-pyramids-and-volcanoes>, accessed May 28, 2025.
- [24] J. H. Hubbell and S. M. Seltzer, *Tables of X-Ray Mass Attenuation Coefficients and Mass Energy-Absorption Coefficients (version 1.4)*, National Institute of Standards and Technology (NIST), Gaithersburg, MD, 1995.
- [25] C. Piemonte and A. Gola, *Overview on the main parameters and technology of modern Silicon Photomultipliers*, Nuclear Instruments and Methods in Physics Research Section A, vol. 926, pp. 2–15, 2019.
- [26] Particle Data Group, *Atomic and Nuclear Properties of Lead (Pb)*, <https://pdg.lbl.gov/2015/AtomicNuclearProperties/HTML/leadPb.html>, accessed May 2025.